

Highlights

Simulating building integrated photovoltaic facades: Comparison to experimental data and evaluation of modelling complexity

Juliana E. Gonçalves, Twan van Hooff, Dirk Saelens

- Building integrated photovoltaic models with varying levels of complexity
- Systematic comparison to experimental data
- Field data from a realistic building integrated photovoltaic setup
- Importance of physics-based thermal-airflow modelling
- Recommendations for building integrated photovoltaic modelling

Simulating building integrated photovoltaic facades: Comparison to experimental data and evaluation of modelling complexity

Juliana E. Gonçalves^{a,b}, Twan van Hooff^{a,c}, Dirk Saelens^{a,b}

^a*Department of Civil Engineering, Building Physics Section, KU Leuven, Leuven, Belgium*

^b*EnergyVille, Genk, Belgium*

^c*Department of the Built Environment, unit Building Physics and Services, Eindhoven University of Technology, Eindhoven, The Netherlands*

Abstract

Building integrated photovoltaic (BIPV) systems provide an opportunity for renewable energy generation in the built environment. In order to quantify the BIPV potential, numerical models of varying levels of complexity have been developed. This paper investigates how the complexity of BIPV models affects their predictions. The study starts with a detailed multi-physics BIPV model that combines a high-resolution one-diode model with physics-based thermal and airflow models. Next, simplifications are introduced into the model. The model predictions are compared to experimental data from a BIPV curtain wall installed in a test building in Leuven, Belgium. The results show that the detailed BIPV model is capable of estimating the BIPV daily energy yield with an average difference of 6.2 % (2.0 % for clear sky days) and the back-of-module temperature with an average difference of 1.74 °C. The use of a linear power model instead of a high-resolution one-diode model affects the average differences, but not significantly: 8.7 % for daily energy

yield predictions (4.5 % for clear sky days) and 1.71 °C for temperature predictions. The use of two different empirical temperature correlations instead of a physics-based approach increases the average temperature difference to 3.5 and 4.4 °C. The average difference in daily energy yield increases to 10.2 and 10.4 %, respectively (5.9 and 5.5 % for clear sky days). These findings indicate that the detailed version of multi-physics BIPV model provides the best agreement with experimental data, but it is still possible to reduce the model complexity with acceptable accuracy.

Keywords: Building integrated photovoltaic (BIPV), Built environment, Facades, Field data, Solar energy, Renewable energy

1. Introduction

One of the major challenges concerning the mitigation of climate change effects is the reduction of the energy consumption and CO₂ emissions related to the building sector. For this reason, the building sector is at the core of energy policies in several countries [1–3]. Within the European Union (EU), the Energy Performance of Buildings Directive (EPBD) states that all new buildings have to comply with the near zero energy building (NZEB) concept by 2020 [4]. The recent EU Clean Energy package substantiates the targets for renewable energy and energy efficiency, with a particular focus on energy performance in buildings [5]. Tackling energy issues in the built environment generally involves three actions [6]: (1) improving the thermal performance of the buildings, while (2) providing renewable energy to cover their remaining energy demand and (3) adopting more energy-efficient end-use appliances.

Photovoltaic (PV) systems are considered a key technology to comply with building energy regulations [7], contributing to increase the renewable energy share in the built environment. PV systems are normally used in the built environment as additional elements attached to the building envelope, the so-called building applied photovoltaics (BAPV). BAPV modules are mounted on supporting structures that are, in turn, attached to the building [8]. BAPVs are often installed on the roof of buildings [8], in an arrangement that does not necessarily follow the existing architecture [9]. For aesthetic reasons, BAPVs are not common in building facades [10].

A promising solution to cope with the aesthetic concerns related to BAPV is the incorporation of PV as a building material, a concept defined as building integrated photovoltaic (BIPV) [8, 11]. Rather than being added to the

building, BIPV elements are part of the building envelope, which facilitates their assimilation into the building architecture [8, 9, 12]. BIPV elements are fundamentally multifunctional, generating electricity while performing one or more functions of conventional building elements, such as thermal insulation, weather tightness, sun shading, and/or acoustic insulation. This multifunctionality is particularly interesting for building renovations, since the integration of PV cell/films in high performance building components offers the possibility to improve the building energy performance and increase the share of renewable energy in the built environment [10, 12, 13].

Over the recent years, a significant research effort has been invested into the development of BIPV models, as reviewed in [14–17]. Yet, only a few studies compare different BIPV models. A comparison between BIPV models for roof applications is presented in [18]; however, the analysis focuses on thermal aspects only. Guidelines for BIPV modelling and simulation in the context of building simulations are also scarce in the literature. The work in [19] describes important phenomena affecting the BIPV performance and suggests improvements for BIPV modelling. However, these suggestions are not verified against experimental data. A recent comprehensive report by the Photovoltaic Power Systems Programme (PVPS) of the International Energy Agency (IEA) reviews existing tools for BIPV design and simulation [20]. Their focus is on the BIPV value chain, including BIPV-specific tools and PV design tools adapted for specific BIPV cases. However, building performance simulation (BPS) tools are not considered.

The present paper evaluates BIPV models with varying degree of complexity through a systematic comparison to experimental data. The focus

is on building performance simulations. The comparative analysis starts with a detailed multi-physics BIPV model proposed previously by the authors [21]. The combination of the following key features distinguishes the multi-physics BIPV model from BIPV models available in the literature: (1) high-resolution electrical modelling, enabling the simulating shading effects inter and intra-module; (2) detailed physics-based thermal and airflow modelling, enabling the simulation of different BIPV configurations; (3) thermal coupling between the BIPV module and the building indoor environment, enabling the assessment of the whole building performance.

Next, simplifications are introduced to the detailed multi-physics BIPV model. The impact of each intervention is quantified and compared to the experimental data. Both electrical and thermal aspects are analysed. The first simplification replaces the high-resolution diode-based model by a linear power model, while the second simplification replaces the physics-based thermal and airflow model by empirical temperature correlations proposed in the literature for BIPV facades. A third approach that only considers the irradiance level and the nominal efficiency of the BIPV module is taken as reference, as it requires the least amount of information. Additional analyses quantify the impact of different assumptions for the modelling of shading effects intra-module, the influence of the maximum power point tracker algorithm on the model predictions, and the impact of increasing the airflow rate on the BIPV performance. From these analyses, recommendations for BIPV modelling in the context of building performance simulations are drawn.

The relevance of this analysis lies in the progressive assimilation of dynamic building simulations by consulting and engineering companies due

to the need to comply with building energy regulations and certificates. The process of designing a building is usually constrained by both time and data/information availability (at least at the beginning of the process). Given these constraints, this paper addresses the question of whether it would be possible to reduce the complexity of BIPV models without compromising its predictions, and what would be the implications of choosing one modelling approach over the other. To the best knowledge of the authors, such systematic comparison including experimental data to evaluate BIPV models in the context of building performance simulations has not been presented yet, in particular, using both electrical and thermal measurements. Another important aspect of this paper is the use of experimental data from a real-size BIPV curtain wall element integrated into a test building. The building integration guarantees realistic interior and exterior operating conditions (e.g. realistic outdoor and indoor temperature conditions, realistic wind flow around the building). Such realistic experimental setup in terms of size and building integration is not common in BIPV research studies. BIPV setups are not always real-size BIPV modules, e.g. [22–24], nor part of a realistic building structure, e.g. [18, 22–26].

The paper is organised as follows. Section 2 describes the BIPV curtain wall element, including the experimental instrumentation and the measuring campaign. Section 3 describes the multi-physics BIPV model and compares the model predictions to the experimental data from the BIPV setup described in Section 2. Next, Section 4 investigates how the model complexity influences its predictions and provides recommendations for BIPV modelling and simulation. Finally, Section 5 discusses the limitations of this work and

Section 6 concludes the paper.

2. BIPV experimental setup

2.1. BIPV curtain wall element

The BIPV component investigated in this paper consists of a full-size curtain wall (CW) element. CW elements are non-load bearing components, which means that they do not provide structural support to the building. Instead, a freestanding structural frame constructed with beams and columns carries the structure load of the building. Such construction type enables the realisation of multi-story high-rise buildings, which are mostly used for commercial or office activities. Being able to exploit the facades of buildings for energy generation has two important advantages. First, the roof area available for energy generation may not be sufficient to cover the building energy demand, not only in commercial buildings [27], but also in multi-store residential buildings [13]. Second, the vertical inclination of building facades profile a more uniform generation profile over the day, helping to balance the mismatch between supply and demand [28, 29].

The BIPV-CW was assembled by a facade constructor taking into account the requirements for building envelope components (air and rain tightness, thermal insulation, aesthetics, fire resistance, etc.). As indicated in Figure 1a,b, a commercial-size PV module composes the top part of the element, while a triple-glazing argon-filled window composes the bottom part (see dimensions in Figure 1d). The BIPV element presents a naturally-ventilated cavity with lateral ventilation openings, as shown in Figure 1c. To ensure realistic operating conditions, the BIPV-CW element is integrated into the

southwest facade of the Vliet test building in Leuven, Belgium ($50^{\circ}52'$ N, $4^{\circ}41'$ E), as shown in Figure 2a. The Vliet building is an isolated low-rise building with a rectangular footprint (Figure 2b), mostly free of shading from the surroundings.

The schematic representation of the BIPV-CW element is presented in Figure 1d. The following four layers compose the upper part of the BIPV-CW (from the outside to the inside): glass-glass PV module, air cavity, insulation panel and plywood panel. The air cavity is 7 cm deep; eight circular openings (1 cm in diameter each) located at the lateral sides of the frame allow the ambient air to flow through the cavity (Figure 1c). The insulation consists of a 15 cm layer of mineral wool. The plywood is 2 cm thick and is used for finishing purposes. Note that the BIPV-CW element is insulated over its perimeter to reproduce the realistic situation in which the element is part of a full building facade.

The PV module used in the BIPV curtain wall is composed of 60 monocrystalline silicon (c-Si) solar cells encapsulated in a transparent EVA (ethylene vinyl acetate) layer at the front and a black EVA layer at the back. The encapsulated cells are covered by 4 mm glass layers at the front and at the back. The power output of the module was measured as 244 W under standard test conditions (STC). The PV module characteristics are summarised in Table 1.

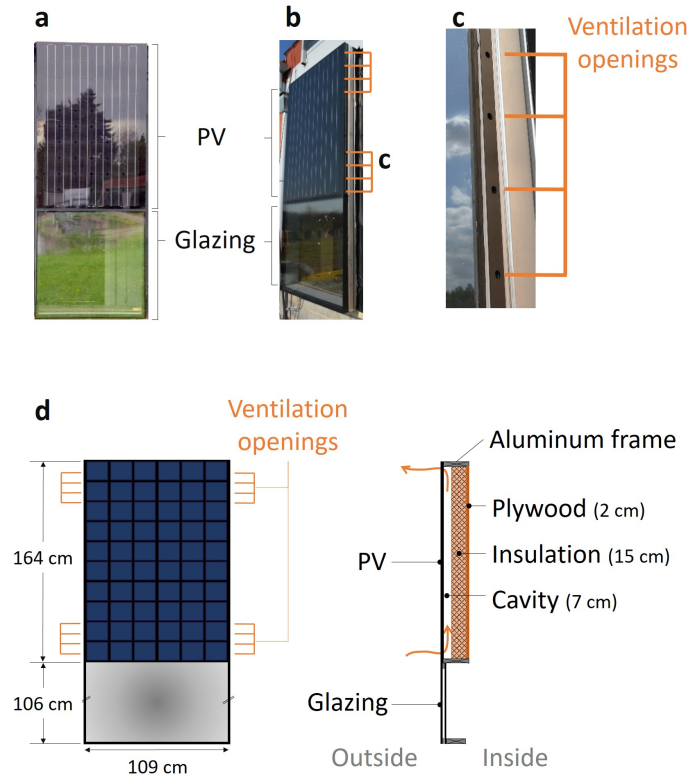


Figure 1: The BIPV-CW element: (a) front picture, (b) side picture, (c) ventilation openings, and (d) front and mid-section schemes of the BIPV-CW element.

Table 1: Characteristics of the PV module.

Measured power at STC (P_{STC})	244 W _P
PV module area (A_{module})	1.09 x 1.64 m ²
Current temperature coefficient (α_T)	0.05 %/K
Voltage temperature coefficient (β_T)	-0.33 %/K
Power temperature coefficient (γ_T)	-0.42 %/K

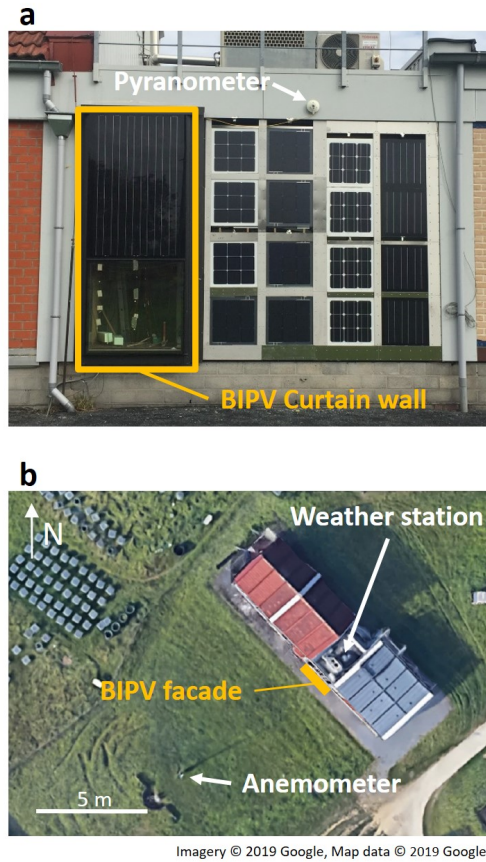


Figure 2: (a) The BIPV facade of the Vliet test building with the BIPV-CW indicated by the yellow rectangle. Note that the facade includes other BIPV modules, which are not considered in this paper. (b) Surroundings of the Vliet test building (Google maps).

2.2. Instrumentation

The BIPV setup provides measurements to characterise both the weather conditions and the BIPV performance (measured power and temperature). The weather dataset is an input to the BIPV model to estimate the BIPV performance (predicted power and temperature). Predictions of power and temperature are then compared to the measurements. Table 2 summarises

the characteristics and accuracy of the measurement equipment. Further information about the measurements are given next.

2.2.1. Weather conditions

The weather data consists of irradiance, ambient temperature and wind conditions. A meteorological station on the building roof records the ambient temperature every one minute (Figure 2b). The wind speed and direction are recorded every five minutes by a ultrasonic anemometer installed at 10 m above the ground and approximately 20 m from the BIPV facade (Figure 2b). The ultrasonic anemometer was replaced by a new one in November 2018. A pyranometer located next to the BIPV-CW measures the solar irradiance on the facade every ten seconds (as indicated in Figure 2b, the pyranometer is installed in a vertical position with its back against the facade). Note that, in order to be used as input data in the BIPV model, the weather variables with a time resolution higher than 10 s are interpolated using Akima splines such that the first derivative is continuous.

2.2.2. BIPV performance

Commercial equipment from Femtogrid Energy Solutions is used to control the BIPV-CW operation. A Femtogrid Solar Power Optimiser PO330 keeps the module at maximum power point (MPP) and increases the output voltage to feed the power to the DC/AC Femtogrid Inverter 2400. From the inverter, the power is injected into the grid. The Femtogrid Inverter 2400 is rated for an input DC power range between 500-3000 W. Since the output power of the BIPV-CW element ranges from 0 to 240 W, the inverter operates below 10 % of the rated input power, resulting in a lower efficiency. For

Table 2: Characteristics and accuracy of the measurement equipment.

Variable	Equipment/Sensor	Time resolution	Accuracy	
Ambient temperature	Hygroclip 2L	60 s	± 0.2 °C	
Wind speed (2004-Nov/2018)	Ultrasonic anemometer Gill Windmaster	300 s	0-20 m/s	1.5 %
			20-35 m/s	1.5-3 %
			35-60 m/s	3 %
Wind direction (2004-Nov/2018)	Ultrasonic anemometer Gill Windmaster	300 s	<25 m/s	$\pm 2^\circ$
			>25 m/s	$\pm 4^\circ$
Wind speed (Nov/2018-Apr/2020)	Ultrasonic anemometer Thies Clima	300 s	≤ 5 m/s	0.1 m/s rms
			>5 m/s ≤ 35 m/s	1 % rms
			>35 m/s ≤ 65 m/s	2 % rms
Wind direction (Nov/2018-Apr/2020)	Ultrasonic anemometer Thies Clima	300 s	>1 m/s ≤ 35 m/s	$\pm 1^\circ$
			>35 m/s ≤ 65 m/s	$\pm 2^\circ$
			>65 m/s ≤ 85 m/s	$\pm 4^\circ$
Solar irradiance	Thermopile pyranometer type CMP Kipp & Zonen	10 s	<3 %	
Surface temperatures	Thermocouple Type T Class 1	1 s	± 0.5 °C	
BIPV power	PO330 rated 300 W DC	~ 2 s	<1%	

this reason, the AC energy fed into the grid is not considered in this study. Instead, this work focuses on the DC power provided by the PV module to the power optimiser, which is recorded (approximately) every two seconds (measured by the same equipment).

As presented in Figure 3, the temperature at different positions over the

BIPV-CW module is monitored using type-T surface contact thermocouples. The following three surfaces are defined (Figure 3b): (S1) back-of-module glass surface (inside the cavity); (S2) insulation layer (inside the cavity); (S3) plywood layer (facing the building interior). On each layer, twelve thermocouples are attached (Figure 3c): five on the right side (R), five on the middle (M), and two on the left side (L). The thermocouples are distributed uniformly over the height (4 to 8 in Figure 3a,c). The thermocouples are of Type T Class 1, with a standard accuracy of ± 0.5 °C, as presented in Table 2). All surface temperatures are recorded every second.

Extra care was taken during the installation of the thermocouples. As recommended in [30–33], the following measures have been taken to mitigate installation errors: the thermocouples were tightly attached to the surface (using a small amount of tape) to reduce contact errors, and the wires of the thermocouples were placed parallel to the respective expected isotherm (at each vertical position).

2.3. Measuring campaign

Experimental data from five periods are used in this paper, a total of 127 days. The climatic conditions recorded over these periods are summarised in Table 3. The dataset includes both clear sky and overcast days, as well as summer and winter conditions. It should be noted that the verification of physics-based models is less dependent on a large dataset (in opposition to data-driven modelling approaches).

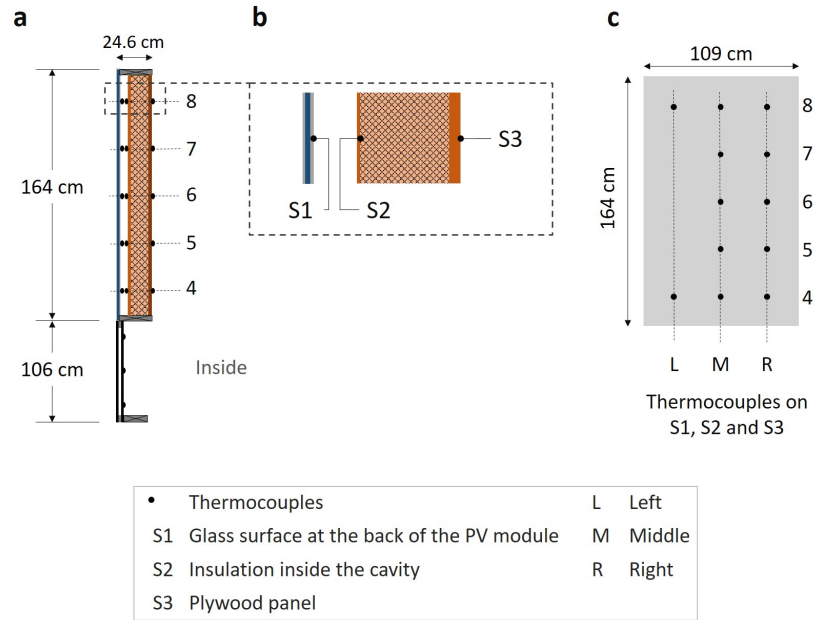


Figure 3: Thermal characterisation of the BIPV-CW element: (a) mid-section view with vertical identification of thermocouples (see Figure 1d), (b) detail indicating the surfaces S1, S2 and S3, and (c) Thermocouples network on each of the surfaces S1, S2, and S3.

Table 3: Weather conditions during the measuring campaign.

		May/18	Jan/20	Feb/20	Mar/20	Apr/20
Total number of days		24	27	22	26	28
Number of clear sky days		7	3	2	10	17
Solar irradiation [W/m ²]	Average	146.1	83.4	102.0	201.2	285.2
	Maximum	907.5	722.1	931.4	981.7	899.6
Ambient temperature [°C]	Average	18.9	6.5	8.0	7.7	12.8
	Maximum	30.4	13.5	18.2	17.7	25.8
	Minimum	3.8	-2.2	-0.9	-2.7	-2.3
Wind speed [m/s]	Average	0.9	2.3	3.4	2.5	1.7
	Maximum	5.0	7.2	10.3	7.0	6.1

3. Multi-physics BIPV model

The multi-physics BIPV model combines a high-resolution electrical model to physics-based thermal and airflow models. The combination of the following key features distinguishes the multi-physics BIPV model from BIPV models available in the literature: (1) high-resolution electrical modelling, enabling the simulating shading effects inter and intra-module; (2) detailed physics-based thermal and airflow modelling, enabling the simulation of different BIPV configurations; (3) thermal coupling between the BIPV module and the building indoor environment, enabling the assessment of the building performance. Furthermore, the model was developed as an external building wall component within IDEAS library, a Modelica-based library for transient simulations of thermal and electrical systems at both building and feeder level [34, 35]. The building models available in IDEAS are described in [35], including an updated intercomparison with BESTEST and a verification based on IEA EBC Annex 58.

Figure 4 illustrates the coupling between the electrical and thermal models is achieved by using the PV temperature ($T_{PV,1}$, $T_{PV,2}$, ..., $T_{PV,n}$) to calculate the power output in the electrical model, which is in turn imposed as a heat sink on the PV layer (P_1 , P_2 , ..., P_n). The airflow through the BIPV cavity (\dot{m}) couples the thermal and airflow models. Figure 4 further illustrates how the BIPV model is coupled to the building model ($T_{int,1}$, Q_1 ; $T_{int,2}$, Q_2 ; ...; $T_{int,n}$, Q_n). The resulting system of equations is iteratively solved by the multi-step solver DASSL with a default tolerance of 10E-04 for the state variables.

The multi-physics BIPV model is based on the modelling approach pre-

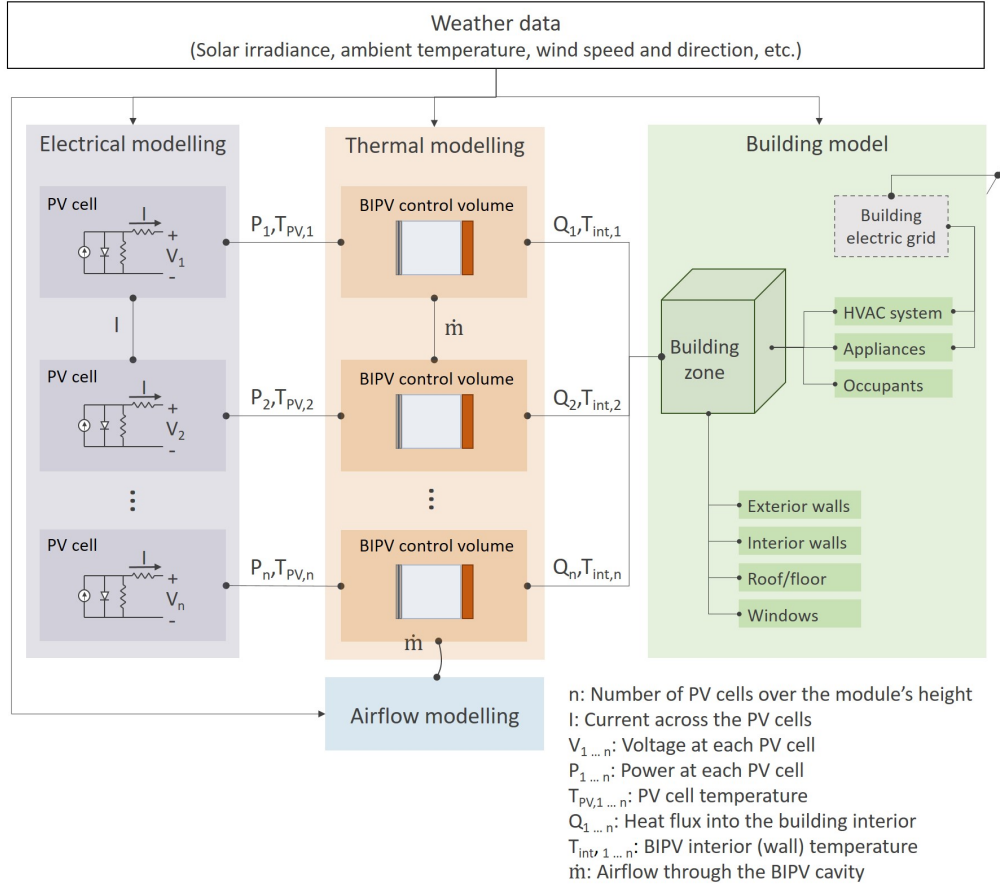


Figure 4: BIPV modelling approach (adapted from [21]).

sented earlier by the authors in [21]. In this previous work by the authors, the modelling approach was used to model a different BIPV configuration (a well-ventilated mini-module with 18 c-Si cells). In order to model the poorly ventilated BIPV-CW in the present work, a new airflow model was developed. The thermal and electrical models remain the same, but are adapted to the size and material characteristics of the BIPV-CW element. The next subsections describe the thermal, airflow and electrical models, focusing on

aspects that are relevant for the present paper. A detailed description of the modelling approach can be found in [21].

3.1. Thermal modelling

The BIPV thermal conditions are defined by the balance between the incoming solar irradiance, the power conversion, the heat transfer to the exterior environment, the heat transfer to the building interior, and the airflow caused by natural ventilation. Figure 5 shows the main variables and heat transfer fluxes defining a BIPV control volume in the multi-physics BIPV model. The control volume includes the PV module, the cavity, and the building wall (which consists of an insulation layer). Table 4 presents the material properties used in the simulations.

The exterior heat transfer is composed of convective heat transfer between the exterior surface and the ambient air ($Q_{c,ext}$) and radiative heat transfer between the exterior surface and both the sky dome ($Q_{r,sky}$) and the ground ($Q_{r,gr}$). Similarly, the interior heat transfer is composed of convective heat transfer between the interior surface and the interior air ($Q_{c,int}$) and radiative heat transfer between the interior surface and the other surfaces composing the building zone ($Q_{r,int}$). Inside the cavity, convective heat transfer occurs between the air volume and the cavity surfaces ($Q_{cav,1}$ and $Q_{cav,2}$) and radiative heat transfer occurs between the cavity surfaces ($Q_{r,cav}$). All the heat exchanges in Figure 5 are described in detail in [21].

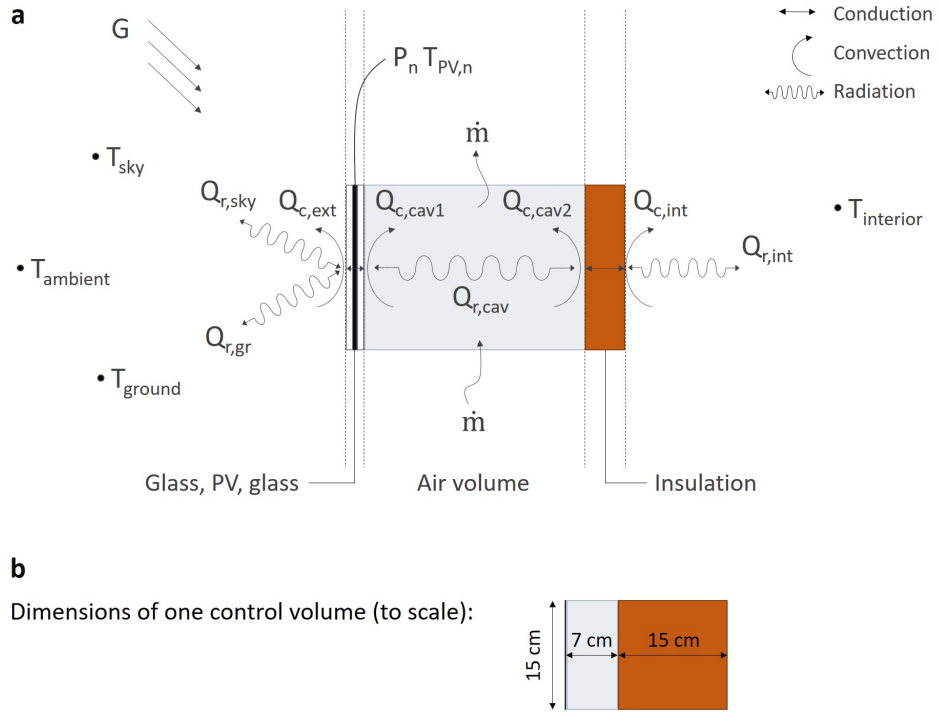


Figure 5: (a) BIPV control volume, where G is solar irradiance, P is power, T is temperature, Q represents the different heat transfer flux, and \dot{m} is the airflow rate (not to scale; adapted from [21]). (b) Main dimensions of one control volume (to scale, for reference).

Table 4: Material properties of the BIPV module.

	Glass	PV cell	Mineral wool
Thickness [m]	0.003	0.0001	0.15
Thermal conductivity [W/mK]	0.96	710	0.036
Specific heat capacity [J/kgK]	750	710	840
Density [kg/m ³]	2500	2330	110
Solar absorptivity [-]	0.95	-	-
Long-wave emissivity [-]	0.9	-	0.8

3.2. Airflow modelling

As illustrated in Figure 4, the airflow through the BIPV cavity interconnects the BIPV control volumes. To estimate the airflow rate, \dot{m} , a power law is used:

$$\dot{m} = \rho_a Q = C \Delta P^n \quad (1)$$

where Q is the volumetric flow rate, ρ_a is the air density, ΔP is the driving pressure differential, C is the flow coefficient and n is the flow exponent. C and n define the so-called pressure characteristics of the BIPV element.

In this work, C and n are obtained using the hydraulic network method. The method defines the total pressure drop over the BIPV element, ΔP_{cav} , as a function of the volumetric flow rate, Q , as follows [36, 37]:

$$\Delta P = \psi \frac{\rho_a Q^2}{2} \quad (2)$$

where ψ is a coefficient that represents all pressure losses in the BIPV element and ρ_a is the air density.

The hydraulic network method divides the BIPV module in a sequence of resistances, which represent friction losses and local losses (e.g. openings). By definition, ψ represents this sequence of resistances, including friction and local losses, as follows [36, 37]:

$$\Delta P = \left(\lambda \frac{H}{D_h} \left(\frac{1}{A_c} \right)^2 + \sum_{i=1}^k \zeta_i \left(\frac{1}{A_i} \right)^2 \right) \frac{\rho_a Q^2}{2}, \quad (3)$$

where the first term inside the brackets corresponds to the well-established Darcy-Weisbach formula to estimate friction losses, with λ the friction factor, H is the cavity height, D_h is the cavity hydraulic diameter, and A_c is the cavity cross-sectional area. The second term concerns the sum of the k local

losses occurring in the cavity, where ξ_i and A_i are the loss factor and the equivalent area, respectively, corresponding to each local loss. For more information about the hydraulic network method, the reader is addressed to [36, 37].

For the BIPV-CW element, local losses are caused by the pressure drop at the openings on each side of the element (Figure 1b,c). An equivalent resistance is defined to represent the four openings at the bottom and the four at the top, each one corresponding to four resistances in parallel (i.e. $\xi_{eq}=\xi_{op}/4$). This assumption is reasonable since the distance between the individual orifices is significantly smaller than the distance between top and bottom of the cavity (a few centimetres vs. 1.5 m). In addition, in view of the important local loss caused at these small openings, further friction losses inside the cavity are assumed negligible.

For each side of the BIPV-CW element, with an equivalent opening at the bottom and another one at the top ($2 \xi_{eq}$), Equation 2 becomes:

$$\Delta P = 2\xi_{eq} \left(\frac{1}{A_{op}} \right)^2 \frac{\rho_a Q^2}{2} \quad (4)$$

where A_{op} is the opening area. This equation describes the airflow at one of the sides of the BIPV-CW element. The total airflow is twice the value obtained from Equation 4, which is then assumed uniform in the cavity.

The losses at one opening, ξ_{op} , can be generally expressed as a function of the driving pressure, ΔP [37]:

$$\xi_{op} = \frac{2}{\rho_a C_d^2 \Delta P^{2n-1}} \quad (5)$$

where C_d is the discharge coefficient, which represents the cavity (friction

and turbulent) losses, and n is the flow exponent, which represents the flow regime (laminar or turbulent).

With a diameter of 10 mm as described in Section 2.1, the ventilation openings in the BIPV-CW are considered as sharp-edged orifices. For sharp-edged orifices, $C_d = 0.611$ and $n = 0.5$ have been theoretically determined by Kirchhoff for turbulent flow [38, 39]. The work in [39] demonstrates experimentally that these values apply to orifices with a ratio length/diameter smaller than 0.25, which is the case for the BIPV-CW element.

The airflow driving pressure is caused by two distinct effects: wind and buoyancy effects. In the multi-physics BIPV model, the resulting buoyancy-induced pressure is computed over all the air volumes in Figure 4, using the following equation:

$$\Delta P_b = g \left[\rho_{\text{ext}} H - \sum_{i=1}^n \rho_i h_i \right] \quad (6)$$

where g is the gravity force, ρ_{ext} is the exterior air density, H is the total height of the air column inside the cavity, ρ_i is the air density of each BIPV control volume, and h_i is the height of each BIPV control volume of a total of n control volumes. The air volumes are considered as well-mixed volumes.

In the BIPV-CW element, the ventilation openings are relatively sheltered from the wind flow due to their position on the sides of the BIPV-CW element as shown in Figure 1. For this reason, wind effects are not considered as a driving force for the cavity flow and only buoyancy is modelled. Note that in this work, the wind effects on the exterior convective heat transfer are considered and take into account the wind speed and direction, as well as the building geometry and building surface (roof and windward, leeward, and side facades) [21].

3.3. *Electrical modelling*

With a good compromise between simplicity and accuracy [40–42], the one-diode model is adopted in this work. As illustrated in Figure 4, each PV cell is described by an individual diode-based circuit; the cell-level circuits are connected to each other to compose the electrical model of the BIPV module. Such high-resolution approach enables the simulation of intra-module shading effects and provides the possibility of including e.g. bypass diodes between strings. This approach has been used before. However, it has been used either in combination with a simplified thermal model (e.g. [22, 43–47]), or for the simulation of stand-alone PV modules (e.g. [43, 44, 48, 49]), while this paper uses a detailed physics-based model to estimate the PV cell temperature and employs the model to simulate a BIPV-CW element.

The power extracted from a PV module depends on the load connected to it. In real applications, a maximum power point tracker (MPPT) is used to maximise the power output by varying the load connected to the module. To simulate the MPPT, this work employs a perturb-and-observe (P&O) algorithm based on [50]. The P&O algorithm adjusts the PV electric operating point according to a given time step. The one-diode model parameters used for a single cell are presented in Table 5. For a detailed description of the electrical model, the reader is addressed to [21].

3.4. *Additional assumptions*

As described in Section 2.1, the BIPV-CW element is insulated over its perimeter, which reduces the peripheral heat transfer to the exterior. For this reason, edge effects are not considered in the model. Also, a uniform

Table 5: Single cell one-diode parameters.

Parameter	Value	Unit
Short-circuit current, I_{SC} (measured)	8.6	A
Open-circuit voltage, V_{OC} (measured)	0.63	V
Series resistance, R_S , value for c-Si cells	0.006425	Ω
Shunt resistance, R_{sh} , assumption for c-Si cells	∞	Ω
Ideality factor, m , assumption for c-Si cells	1	-

airflow (both with respect to velocity magnitude and flow direction) is assumed over the width and depth of the cavity (as described in Section 3.2). Consequently, PV cells at a given height have the same temperature, regardless their position at the right, left or at the middle of the BIPV module (R, L or M, respectively). These assumptions are in agreement with the experimental data, which reveal only a minor reduction in temperature from the middle to the sides of the module, indicating that the element is well insulated from the exterior and that the local effects of ventilation on the lateral sides are rather limited. Note that temperature variations over the height of the module caused by ventilation are considered in the model. A final remark is that the building interior is not modelled in detail. Instead, a convective-radiative boundary condition is imposed on the insulation layer (S3 in Figure 3) to represent the heat transfer from/to the building and a constant value of 25 °C is assumed for the interior air temperature. In view of the high thermal resistance of the relatively thick insulation layer, the thermal resistance of the plywood panel is neglected.

3.5. Simulation parameters

As mentioned previously, this work uses a multi-step solver, which means that the solver adapts the time step of the simulation according to the dynamics of the system. Since the MPPT is much faster than the thermal dynamics of the problem, the MPPT ultimately determines the time step of the simulation. In this work, the MPPT is set to operate at the lower time resolution in the weather dataset (i.e. 10 s for solar irradiance input). This means that the simulation time step is also 10 s. Within the 10 s period, the dynamics of the system can be neglected, as will be demonstrated later in Section 4.1.2. Note that the weather inputs with a time resolution higher than 10 s are interpolated using Akima splines such that the first derivative is continuous.

3.6. Comparison to experimental data

3.6.1. Performance indicators

This section evaluates the capability of the multi-physics BIPV model to estimate the daily energy yield and the temperature at different locations of the BIPV-CW element. The daily energy yield values are obtained from the numerical integration of power predictions and measurements. The predicted and measured energy yield values are compared to each other in both absolute and relative terms. The results are presented based on the mean absolute error (MAE), mean relative error (MRE), and relative root mean squared error (rRMSE). Temperature results are presented in terms of MAE and RMSE, since absolute indicators are more appropriate for temperature evaluations. To calculate temperature indicators, the model predictions and

measurements are averaged over one minute. Temperature results are evaluated based on surface-average value as well as at different positions over the BIPV height. Based on the scheme presented in Figure 3c, the surface-average temperature is defined as the average of the thermocouples attached to the surface on the right, middle and left. The thermocouples R5, R6 and R7 are used as approximation for the temperature at the levels L5, L6 and L7, which are not monitored.

3.6.2. Results

Figure 6 compares the multi-physics BIPV model to the measurements for six consecutive sunny days in May 2018. The weather conditions (Figure 6a), the power (Figure 6b) and surface-average temperatures (Figure 6c,d) are shown. For clear sky days, a good agreement between the measurements and the model predictions is visually verified in Figure 6. The average difference in power for these six days is less than 1 W. The average differences in temperature are $-1.8\text{ }^{\circ}\text{C}$ and $-2.1\text{ }^{\circ}\text{C}$ for the back-of-module and insulation surfaces, respectively (S1 and S2 in Figure 3). The measurement accuracy is not shown in Figure 6 for the sake of clarity, but is presented in Table 2.

Next, the daily energy yield is quantified for both the model and the measurements. These results are presented in Figure 7 for 15 consecutive days in May 2018, including the days depicted in Figure 6. For the clear sky days such as May 4-9, the energy yield predictions are fairly close to the measured values (Figure 7). In contrast, the difference between modelled and measured energy yield is relatively higher for cloudy days, such as May 12, 14 and 15.

Table 6 summarises the daily energy yield results for all periods in the

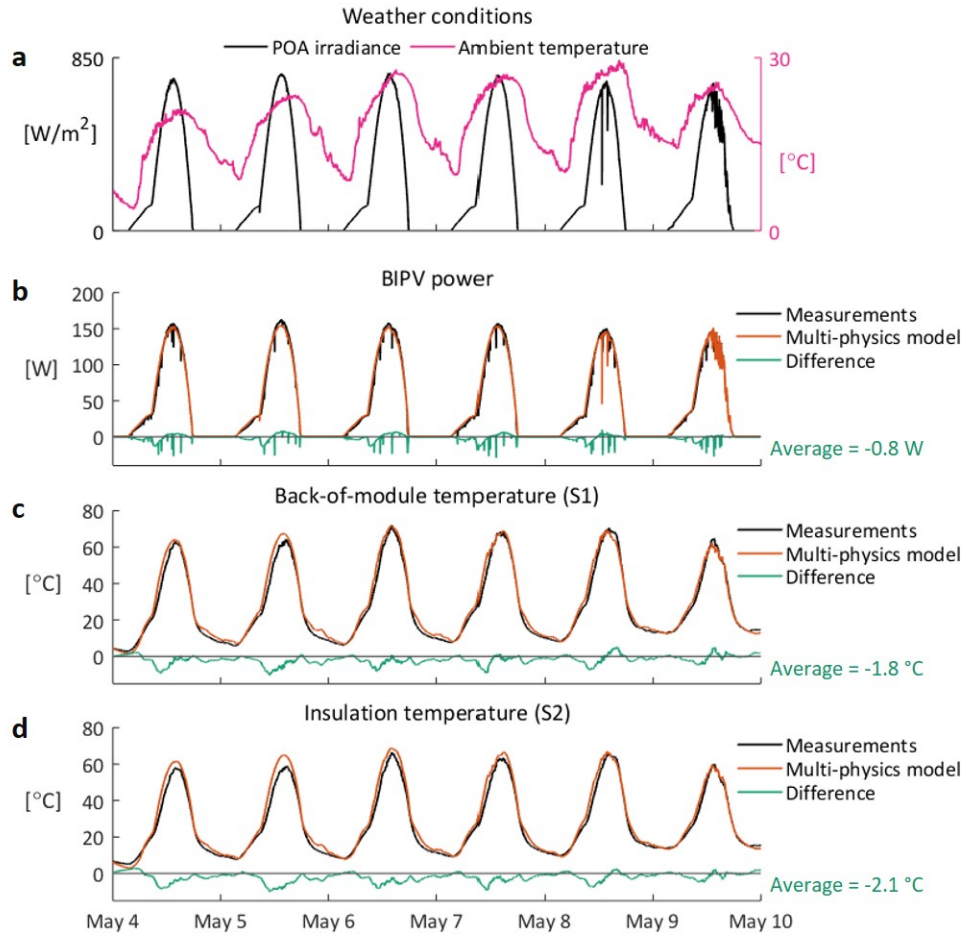


Figure 6: Comparison between multi-physics BIPV model and measurements: (a) plane-of-array (POA) irradiance and ambient temperature, (b) power, (c) back-of-the-module surface-average temperature (S1), and (d) insulation surface-average temperature (S2). In these plots, Difference = (Measurements - Model).

measuring campaign. In general, the average indicators for the daily energy yield predictions are of the same order of magnitude for all periods. MAE values vary between 9.8 and 37.1 Wh, MRE values between 2.3 and 12 %, and rMSE values between 3.0 and 20.3 % (rMSE quantifies the spread of the residuals). January shows slightly lower MAE values, which are related to lower irradiance levels rather than to the model accuracy, as reflected in higher MRE and rRMSE values (Table 6). For the whole dataset, the average MAE, MRE and rRMSE are 19.7 Wh, 6.2 % and 11.0 %, respectively (Table 6). Furthermore, the model performs better for clear sky days. This is evident when relative indicators are compared: clear sky days present a MRE of 2.0 % and rRMSE of 2.6 %, compared to 6.2 % and 12.8 % for the rest of the dataset (Table 6).

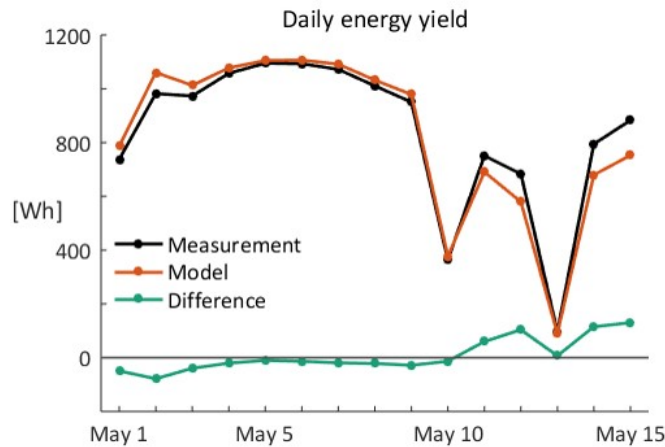


Figure 7: Daily energy yield results for 15 days in May 2018: Comparison between measurements and multi-physics BIPV model. Difference = (Measurements - Model).

Differences in daily energy yield predictions between clear sky and cloudy days may be partially attributed to differences in time resolution between

Table 6: Average daily energy indicators for all periods. The selection of clear sky days was carried out visually, considering days that are similar to May 4-9 in Figure 6

	Energy yield	MAE	MRE	rRMSE
	[Wh]	[Wh]	[%]	[%]
May/18	789.3	37.1	5.0	6.6
Jan/20	213.5	9.8	12.0	20.6
Feb/20	280.8	13.5	6.8	8.3
Mar/20	587.2	21.6	5.2	6.4
Apr/20	893.2	17.6	2.3	3.0
Whole dataset	545.7	19.7	6.2	11.0
Clear sky days	1055.2	20.7	2.0	2.6
Except clear sky days	351.9	19.3	7.9	12.8

the power measurements, which are recorded approximately every two seconds, and the input weather data, particularly the irradiance data, which is recorded with a ten-second resolution. This means that actual variations occurring within this period are not present in the input dataset, resulting in somewhat larger errors for days with highly varying radiation. Another possible cause of deviations is that the model does not differ between diffuse and direct irradiance, since the total irradiance on the facade is used as input.

Figure 8 presents the temperature profiles at the bottom and top of the BIPV-CW cavity, with bottom corresponding to height 4 and top to height 8 (see Figure 3). The temperature of the two cavity surfaces S1 and S2 is shown. This figure shows the measured temperatures and the differences between predictions and measurements; the predicted temperature profiles are not included for the sake of readability. Next, Table 7 summarises the

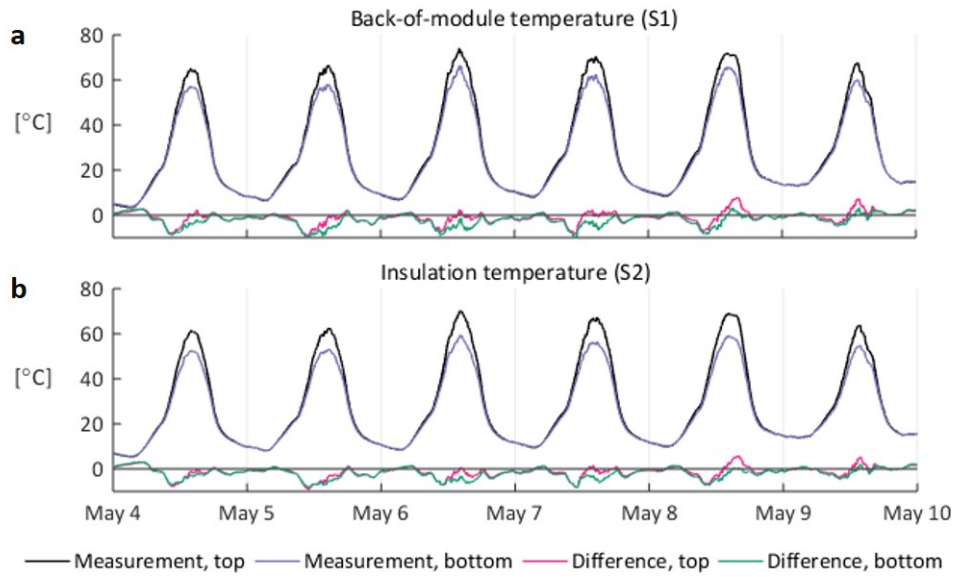


Figure 8: Temperature at the top and bottom of the BIPV-CW module: (a) back-of-module temperature (S1) and (b) insulation temperature (S2). Bottom and top correspond to height 4 and 8 in Figure 3. In these plots, Difference = (Measurements - Model). Note that the predicted temperature profiles are not shown for the sake of readability.

daily average MAE values for the temperature at the top and bottom, as well as for the surface-average temperature (both S1 and S2), for all periods in the dataset. These results show that the model is able to estimate fairly well the temperature at the bottom and at the top for both surfaces composing the cavity, i.e. the back-of-module and the insulation layer. The daily average MAE remains mostly below $2.5\text{ }^{\circ}\text{C}$ and RMSE mostly below $3\text{ }^{\circ}\text{C}$ in all cases (Table 7).

Table 7: Summary of S1 and S2 temperature results: Average MAE and average RMSE (calculated over 1 minute).

Period	Surface-average		Top – M8		Bottom – M4	
	MAE [°C]	RMSE [°C]	MAE [°C]	RMSE [°C]	MAE [°C]	RMSE [°C]
Surface S1: Back of the module						
May/18	1.74	2.50	1.77	2.61	2.04	2.81
Jan/20	1.94	2.38	2.14	2.64	2.40	2.89
Feb/20	1.39	2.07	1.52	2.18	1.74	2.38
Mar/20	1.88	2.83	1.99	2.90	2.22	3.10
Apr/20	1.97	2.76	2.20	3.14	2.14	2.90
Surface S2: Insulation inside the cavity						
May/18	1.83	2.50	1.68	2.38	1.92	2.53
Jan/20	1.85	2.34	1.57	2.03	1.39	2.03
Feb/20	1.17	1.75	1.06	1.71	1.33	2.22
Mar/20	1.84	2.95	1.70	2.90	1.62	2.63
Apr/20	1.93	2.81	1.90	2.74	2.99	4.77

4. Evaluation of model complexity

Starting from the detailed multi-physics BIPV model discussed so far, this section quantifies the impact of two modelling simplifications concerning the electrical and thermal-airflow models. This section also analyses the impact of secondary assumptions/parameters related to the electrical model (shading and MPPT) and thermal-airflow model (ventilation).

4.1. Electrical modelling

For this analysis, the one-diode model in the original multi-physics BIPV model is replaced by a linear power model. The physics-based thermal and airflow models described in Section 3.1 and 3.2 are maintained. This combination is illustrated in Figure 9. In this case, the coupling between thermal and electrical effects still holds. However, the simulation of intra-module shading effects is not possible anymore, because the power model does not consider mismatches between cells.

The power model is based on the following equation:

$$P = \eta_{\text{STC}} \left[1 + \gamma_{\text{T}} (T_{\text{PV}} - 25) \right] GA \quad (7)$$

where η_{STC} is the efficiency at STC, γ_{T} is the temperature coefficient for power, T_{PV} is the PV cell temperature, G is the plane-of-array irradiance, and A is the PV area. The values for η_{STC} and γ_{T} are obtained from Table 1. As illustrated in Figure 9, the cell temperature, T_{PV} , is defined by the thermo-electrical coupling between the physics-based thermal and airflow models and the power model. Note that using the power model at the cell level is not common in the literature, but was needed here for the correct coupling to the physics-based thermal and airflow models.

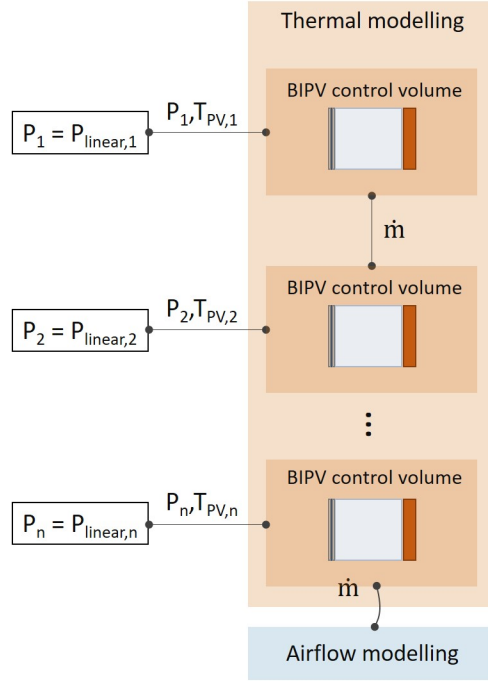


Figure 9: First simplification: power model instead of the one-diode model; physics-based thermal and airflow models remain (in relation to the scheme in Figure 4).

Figure 10 presents the profiles of power and (back-of-module) temperature for four sunny days in May. Figure 11 presents the results in terms of daily energy yield as well as the MAE for the back-of-module temperature. All results are summarised in Table 8. A third model is included in this analysis as reference, where the temperature effects in the power model are not considered (from Eq. 7, $P_{\text{ref}} = \eta_{\text{STC}}GA$).

For the days depicted in Figures 10 and 11, barely any difference is observed between the multi-physics (one-diode) model and the power model. For the whole dataset, the power model presents MAE and MRE values of 29.7 Wh and 8.7 %, respectively (Table 8). These values are higher compared

to the one-diode model MAE and MRE of 19.7 Wh and 6.2 %, respectively (Table 8). With respect to back-of-module temperature (T_{BoM}), both multi-physics (one-diode) model and power models provide equally good results: 1.74 and 1.71 °C. A similar trend is observed for clear sky days, but in this case the errors are relatively smaller for both models. For clear sky days, the power model MAE and MRE values are 47.6 Wh and 4.6 % (compared to 20.7 Wh and 2.0 % for the multi-physics (one-diode) model). In contrast, if temperature effects are not considered (*Power model, no T effects*), the BIPV energy potential is significantly overestimated. At peak power production, differences up to 30 W are observed in Figure 10a (about 20 % overestimation compared to the measurements). With respect to daily energy yield predictions, not considering temperature effects leads to underestimations up to approximately 20 % on sunny days (Figure 11b) and 12.7 % on average (Table 8).

These results suggest that the linear power model (including temperature effects) could be a suitable choice for a non-shaded BIPV module (although with slightly higher errors). The main advantage of employing the power model is the decrease in total simulation time, since a larger time step can be used (will be explained later in Section 4.1.2). However, a power model is not suitable for the simulation of shading effects, since it does not consider mismatch losses. Shading is treated in the next subsection.

4.1.1. Shading effects

This section compares different modelling assumptions to quantify the power loss caused by partial shading. Six cases are defined in Figure 12 to illustrate how shading can be implemented in BIPV models. The case without

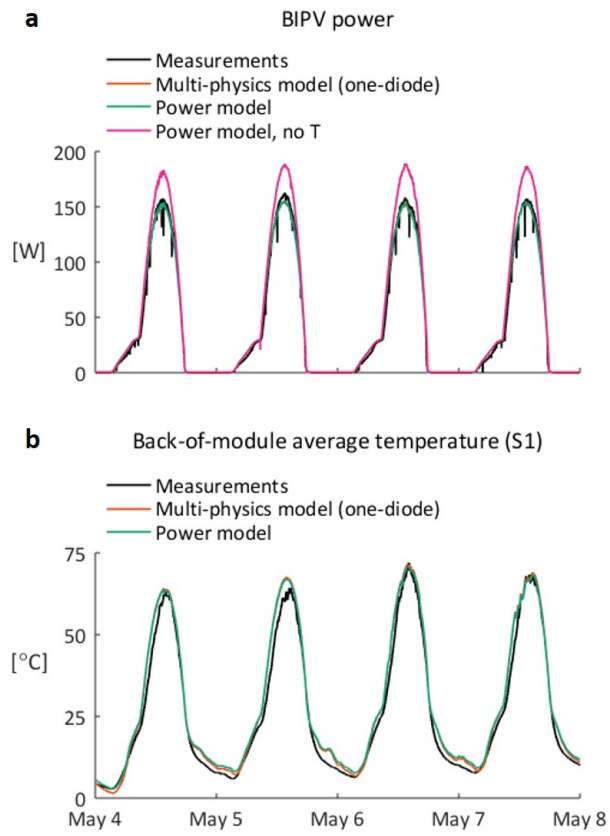


Figure 10: Impact of the electrical model: (a) power, and (b) back-of-module surface-average temperature.

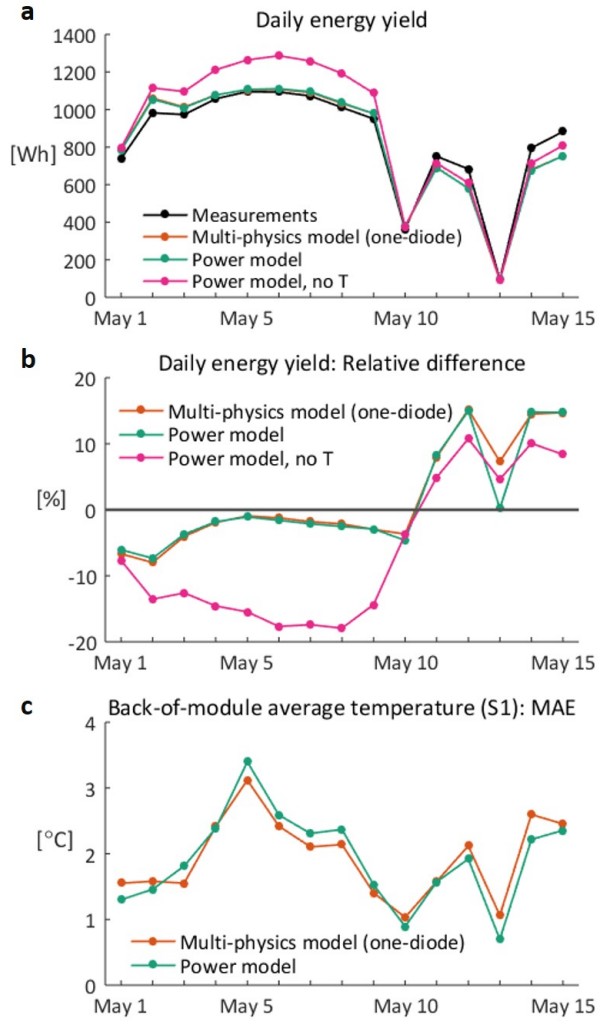


Figure 11: Impact of the electrical model: (a) daily energy yield, (b) difference in daily energy yield between measurements and models, and (c) MAE of back-of-module average temperature

Table 8: Impact of the electrical model: daily energy yield (DEY) and back-of-module temperature (T_{BoM}) predictions (whole dataset and clear sky days).

	DEY	DEY	DEY	T_{BoM}
	Average	MAE	MRE	MAE
	[Wh]	[Wh]	[%]	[°C]
<hr/> Whole dataset <hr/>				
Measurements	545.7	-	-	-
Multi-physics model (one-diode)	542.8	19.7	6.2	1.74
Power model	553.7	29.7	8.7	1.71
Power model, no temperature effects	578.0	53.4	9.0	-
<hr/> Clear sky days <hr/>				
Measurements	1055.2	-	-	-
Multi-physics model (one-diode)	1072.2	20.7	2.0	1.47
Power model	1102.8	47.6	4.5	2.70
Power model, no temperature effects	1188.6	133.4	12.7	-

shading is taken as reference. The first intra-module case (IM1) considers that one string (20 cells) receives 50 % less irradiance, while the other two strings are not shaded. The second intra-module case (IM2) imposes shading on the second string as well: two strings receive 50 % less irradiance and the remaining string is not shaded. The “module level” approach distributes the irradiance equally over all cells in the module, i.e. the irradiance at cell level is averaged at module level. The case module level 1 (ML1) corresponds to the conditions in IM1, while ML2 corresponds to IM2. Last, the conservative (CS) approach considers that all strings receive 50 % less irradiance (i.e. all cells receive the amount of irradiance as the least irradiated cell). These cases are simulated using the multi-physics BIPV model in its original form, i.e. using the high-resolution one-diode model. Note that this is a numerical exercise that uses generic cases to compare shading modelling assumptions.

Figure 13 presents the BIPV power for a clear sky day and the daily energy yield over several days for the cases defined in Figure 12. As expected, the conservative approach (CS) provides the lowest power output, followed closely by cases IM2 and IM1. ML2 and ML1 come next, with higher power outputs. Compared to the reference case, the daily energy yield reduces by about 51 % for the CS case, 48 % for IM1, 45 % for IM2, 17 % for ML1, and 34 % for ML2. These results indicate that the conservative CS case is a rather good approximation for both intra-module cases, predicting a slightly higher reduction in energy yield (about 51 %) compared to the intra-module cases IM1 and IM2 (about 48 % and 45 % reduction, respectively). In contrast, the “equivalent shading” approach does not seem appropriate to represent intra-module cases, as it underestimates the shading effects, with



Figure 12: Generic cases used to illustrate how shading can be implemented in BIPV models.

energy predictions significantly higher compared to the partial shading results (about 17 and 34 % compared to 45 and 48 %). This result is relevant because the CS case can be used with the power model, since all cells operate under the same conditions. The IM cases require the use of an one-diode model to account for current mismatch losses between cells. In turn, the one-diode model requires a MPPT algorithm to find the operating point of the BIPV module, which leads to an increase in total simulation time. If the use of

a one-diode model is necessary for a more accurate simulation of shading effects (or another reason such as the need to obtain the current-voltage characteristics of the module), then the total simulation time becomes an important constraint. The next analysis explains and quantifies the influence of the MPPT algorithm on the simulation time and on the model predictions.

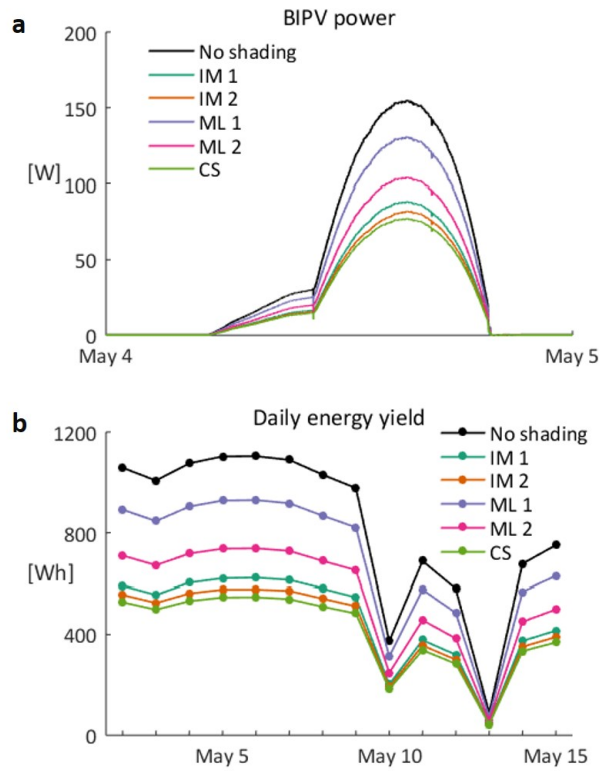


Figure 13: Comparison between modelling approaches to simulate shading effects: (a) power output for a clear sky day, and (b) daily energy yield predictions.

4.1.2. MPPT and simulation time step

As briefly mentioned in Section 3.5 the multi-physics BIPV model employs a multi-step solver. From the multi-step solver perspective, the sam-

pling nature of the MPPT algorithm leads to time events, i.e. moments in time at which the system conditions change. A time event is triggered every time the MPPT algorithm acts on the system (which depends on the MPPT sampling time). At these time events, the entire system of equations needs to be solved, including thermal couplings (between the electrical and thermal model as well as between BIPV and the building). Therefore, the sampling time of the MPPT algorithm ultimately defines the (maximum) time step of the simulation. From now on, the terms sampling time and simulation time step are treated interchangeably.

Ideally, the simulation time step should be able to capture the changes in the input data as well as the dynamics of the problem. However, shorter time steps imply longer calculation periods. The question here is whether it is possible to reduce the total simulation time by increasing the maximum time step (limited by the MPPT sampling time) without compromising the model predictions. For this analysis, four time steps are defined: 10 s, 60 s, 300 s and 600 s. Note that 10 s corresponds to the resolution of the solar irradiation data, 60 s to the ambient temperature, and 300 s to the wind conditions. A time step of 600 s is included as it corresponds to the best resolution of standard weather files for building performance simulations. This analysis is purely numerical, and thus measurements are not included.

Figure 14 shows the total daily energy yield for 14 days in May for all time steps. Table 9 summarises the influence of the time step on daily energy yield predictions and CPU time. The relative differences are calculated based on the reference time step of 10 s. These results indicate that raising the time step from 10 to 60 s barely affects the daily energy yield predictions, with

differences below 0.2 %. The impact on the CPU time is rather significant: the simulation with a time step of 60 s takes only 22 % of the time needed for a simulation with 10 s. The results for 300 s are also acceptable, with average reduction in daily energy yield below 1 % and a further reduction in CPU time by 7 %. The major differences in energy yield predictions occur only when the time step is raised to 600 s, likely due to the loss of information on the dynamics of the system. This result is in agreement with findings in [51] and [52], which highlight the inability of temporal resolutions above 600 s to capture the (BI)PV dynamics.

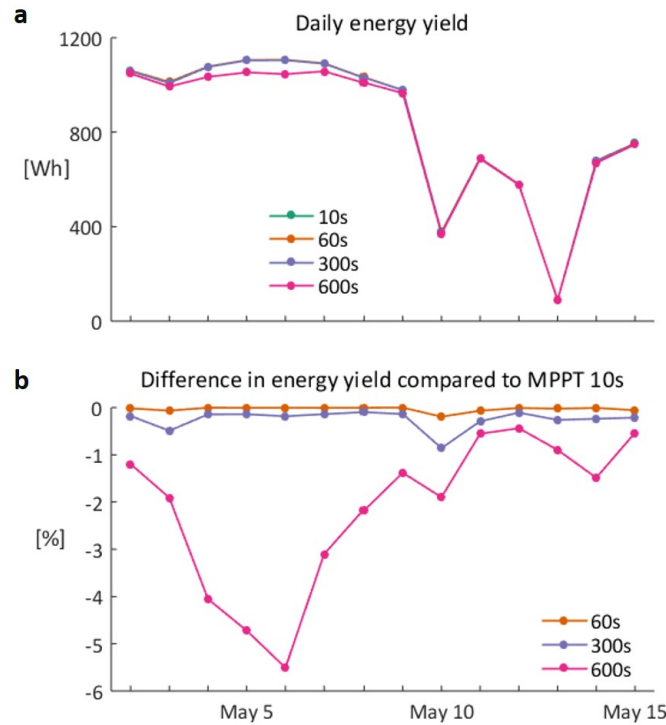


Figure 14: Influence of time step on the model predictions: (a) daily energy yield, and (b) difference in daily energy yield compared to a time step of 10 s.

Table 9: Impact of the time step on daily energy yield predictions and CPU time.

Relative reduction in daily energy yield compared to the reference			
10 s	60 s	300 s	600 s
Reference (100 %)	<0.2 %	<1 %	<6 %
CPU time (percentage with respect to the reference CPU time)			
10 s	60 s	300 s	600 s
Reference (100 %)	22 %	7 %	5 %

4.2. Thermal and airflow modelling

This section investigates whether the thermal and airflow modelling approach used in the multi-physics BIPV model can be simplified. For that, the high-resolution one-diode model described in Section 3.3 is maintained, while the physics-based thermal-airflow model is replaced by empirical correlations from the literature, as illustrated in Figure 15. These empirical temperature correlations provide a single temperature value to represent the whole PV module, which is imposed to all the cells in the electrical modelling to obtain the power output of the module. This means that thermal and electrical models are decoupled. The simulation of intra-module shading effects is still possible, because the high-resolution one-diode model is maintained (i.e. mismatch losses are considered).

Two (semi-)empirical correlations are considered in this paper. The first correlation is the one proposed by Ross et al. [53], which defines the module temperature as:

$$T_{PV} = T_a + kG, \tag{8}$$

where T_a is the ambient temperature, k is an empirical coefficient that depends on the level of integration into the building, and G is the plane-of-array

solar irradiance. For facade integration, a coefficient $k = 0.0538 \text{ } ^\circ\text{Cm}^2/\text{W}$ is proposed in [54] based on the experimental data presented in [55].

The second semi-empirical correlation was proposed by Skoplaki et al. [56]. It includes the influence of the wind speed, being defined as follows:

$$T_{\text{PV}} = T_{\text{a}} + \omega G \left[\frac{0.32}{8.9 + 2V_{\text{f}}} \right], \quad (9)$$

where T_{a} is the ambient temperature, ω is the mounting coefficient, G is the plane-of-array solar irradiance, and V_{f} is the free stream wind speed. For facade integration, a coefficient $\omega = 2.4$ is derived by [56]. Note that ω is derived from k and, therefore, also corresponds to the experimental data presented in [55]. In the present work, the wind speed measured at 10 m height in the open field upstream of the building is used as V_{f} .

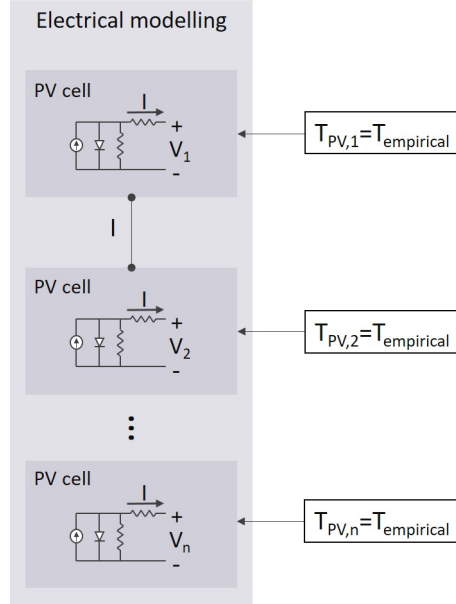


Figure 15: Second simplification: Empirical temperature correlations instead of physics-based thermal and airflow models; one-diode model remains (in relation to Figure 4).

Temperature deviations are presented in Figure 16 for 15 days in May 2018. Results for the back-of-module temperature (T_{BoM}) for the whole data set are summarised in Table 10. The multi-physics model provides the lowest differences in temperature, generally underestimating the measurements (Figure 16b). On average, both empirical temperature correlations present higher MAE for the back-of-module temperature: 3.5 and 4.4 °C for Ross' and Skoplaki et al.'s correlations, respectively, compared to 1.7 °C for the multi-physics model (Table 10).

The values for k and ω used in Ross' and Skoplaki et al.'s correlations correspond to a poorly ventilated BIPV module. This means that both correlations are expected to perform well for BIPV modules operating in similar conditions, i.e. BIPV with poor ventilation, as is the case for the BIPV curtain wall treated in this paper. For clear sky days, such as May 5-9, for which both Ross' and Skoplaki et al.'s correlations provide fairly good temperature estimations (Figure 16c and d). However, for days with highly varying irradiance (such as May 1-3), the Ross' correlation presents temperature deviations up to ± 30 °C from the measurements (Figure 16c). In the case of the Skoplaki et al.'s correlation, differences in temperature can exceed 40 °C (Figure 16d). One reason for that is that Ross' and Skoplaki et al.'s correlations do not consider thermal dynamics. Therefore, variations in the irradiance are directly reflected in their temperature predictions (see Eqs. 8 and 9). For the Skoplaki et al.'s correlation, variations in wind speed also affect temperature predictions, which is particularly visible during clear sky days, such as May 5-9. In contrast, the multi-physics model is a dynamic model, in which fluctuations in irradiance are attenuated by the thermal

capacity of the BIPV-CW module.

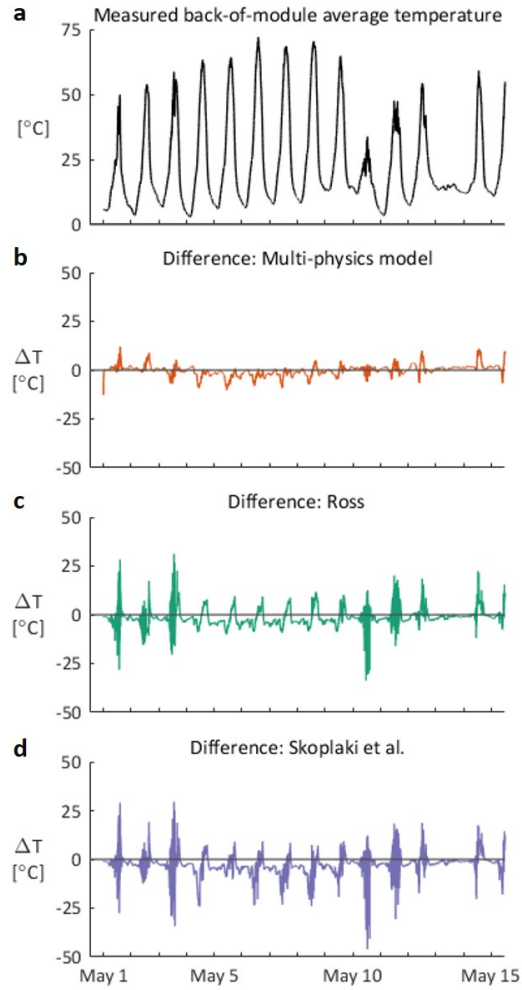


Figure 16: Impact of the temperature model: (a) Measured back-of-module surface-averaged temperature (S_1), (b) temperature difference between the measurements and the physics-based model, and (c,d) same as (b) for the Ross' and Skoplaki's models.

Daily energy yield results are presented in Figure 17. Results for the whole data set are summarised in Table 10. For reference, the results for

the power model without temperature effects are repeated in this section ($P_{\text{ref}} = \eta_{\text{STC}}GA$). The multi-physics model presents the best agreement with experimental data. Ross' and Skoplaki et al.'s correlations present results of the same order of magnitude: MAE of 33.9 and 34.2 Wh, respectively, and MRE of 10.2 and 10.4 %, respectively. For clear sky days, average MRE is below 6 % for both Ross' and Skoplaki et al.'s correlations. Again, not considering temperature effects leads to underestimations up to about 20 % (Figure 17) and of 12.7 % on average (Table 8).

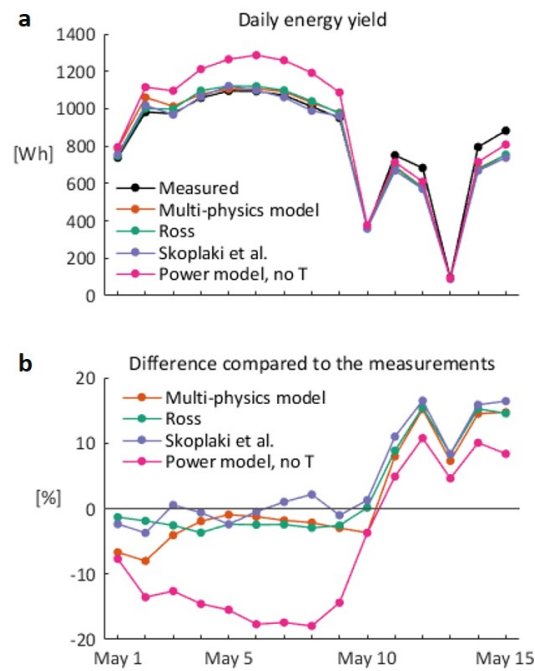


Figure 17: Impact of the temperature model: (a) daily energy yield, and (b) difference in daily energy yield compared to the measurements.

Power as a function of the difference between back-of-module temperature and ambient temperature is presented in Figure 18. It is important to

note that both the multi-physics and the linear power models are combined with physics-based thermal-airflow models, while the multi-physics and Ross and Skoplaki et al.'s correlations are combined with high-resolution one-diode models. These plots show that models using a physics-based thermal-airflow approach are closer to the measurements, while models based on empirical temperature correlations tend to overestimate the PV temperature, which leads to underestimations of power output. The higher temperature estimations are also reflected on the average daily energy yield predicted by these models: 508.5 and 505.4 Wh for Ross and Skoplaki et al.'s correlations, respectively, compared to 542.8 Wh predicted by the multi-physics model and 545.7 Wh calculated from the experimental data (Table 10).

In addition to the deviations in daily energy yield and temperature predictions discussed previously, empirical temperature correlations are not particularly suitable for the simulation of different BIPV configurations. Since ambient temperature and irradiance are the only variables in these empirical temperature correlations, design modifications in terms of material properties or cavity ventilation cannot be simulated. In the next section, cavity ventilation is used as an example to illustrate the advantage of a physics-based approach.

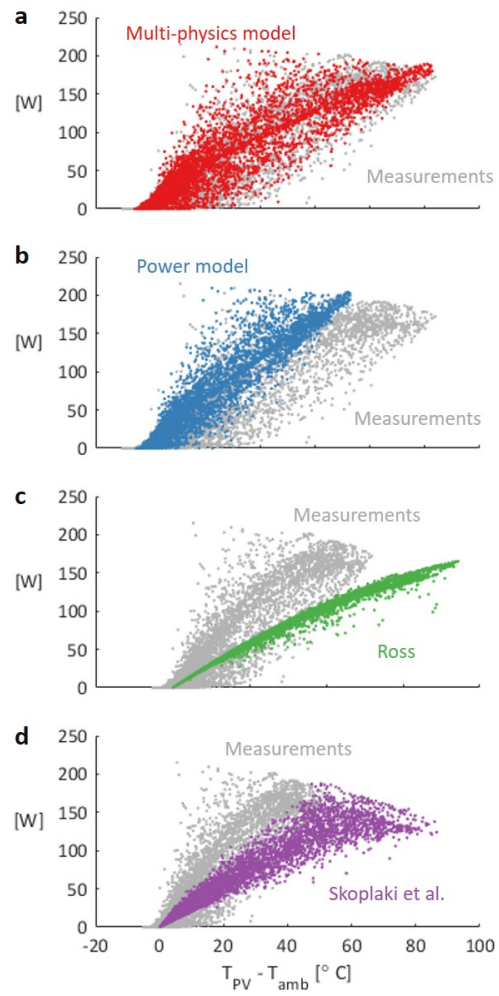


Figure 18: Power as a function of back-of-module surface-average temperature: (a) Multi-physics model, (b) Power model, (c) Ross' correlation, and (d) Skoplaki et al.'s correlation. Data averaged over 10 min.

Table 10: Impact of the temperature model: daily energy yield (DEY) and back-of-module temperature (T_{BoM}) predictions (whole dataset). Results for the power model without temperature effects are included for comparison.

	DEY	T_{BoM}	DEY	DEY
	Average	MAE	MAE	MRE
	[Wh]	[°C]	[Wh]	[%]
Whole dataset				
Measurements	545.7	-	-	-
Multi-physics model (physics-based)	542.8	1.7	19.7	6.2
Ross	508.4	3.5	33.9	10.2
Skoplaki et al.	505.4	4.4	34.2	10.4
Power model, no temperature effects	578.0	-	53.4	9.0
Clear sky days				
Measurements	1055.2	-	-	-
Multi-physics model (physics-based)	1072.2	1.5	20.7	2.0
Ross	1005.7	6.5	62.9	5.9
Skoplaki et al.	1002.4	6.4	58.0	5.5
Power model, no temperature effects	1188.6	-	133.4	12.7

4.2.1. Importance of physics-based modelling

To illustrate the flexibility of a physics-based model, the impact of enhancing ventilation on the performance of the BIPV curtain wall element is presented here. To emulate increasing ventilation rates, the following C values are simulated: 10, 200, 500 and 800 ACH/Paⁿ, where the unit ACH quantifies the cavity air changes per hour (see Equation 1). These C values are in agreement with pressure characteristics of traditional building elements experimentally determined by different authors [21, 37, 57]. For practical building calculations, the use of $n = 0.7$ has been suggested [58, 59], which is adopted in this work. In addition, wind effects are included as driving force in the airflow calculation, assuming that the openings are perpendicular to the wind flow, as explained in [21].

The resulting airflow rate and back-of-module temperature are presented in Figure 19. As expected, a higher C value increases the airflow rate through the cavity (Figure 19a), leading to lower temperatures (Figure 19b). For the clear sky days, a reduction in temperature of about 10 °C is observed for $C = 500$ and $C = 800$ compared to $C = 10$ (Figure 19b). The decrease in temperature leads to higher daily energy yields, as shown in Figure 20. For clear sky days such as May 4-8, an increase in daily energy yield within 2.0-3.7 % is observed when the C value increases from 10 to 200, 500 and 800 (Figure 20b). The most significant increase in daily energy yield is achieved when the C value increases from 10 to 200. The energy gain from $C = 200$ to 500 and then to 800 is relatively lower. Although the increase in daily energy yield might seem relatively small, the decrease in temperature may have a significant impact on the module lifetime: a 1 °C decrease in the operating

temperature could extend the module's lifetime by about 7 %, or 2 years [60]. Moreover, being able to estimate the airflow rate is important for the evaluation of BIPV/thermal (BIPV/T) systems, in which the BIPV module is integrated with other energy systems, such as a heat pump or a drying system.

The Ross' correlation and the power model without temperature effects are included in Figure 20 only as reference, since they do not consider the physical characteristics of the BIPV module. Figure 20a shows that the Ross' correlation is closer to the reference case of $C = 10$, which represents a relatively poorly ventilated BIPV module. In fact, the coefficient k used in the Ross' correlation (Equation 8) was derived from experimental data of a poorly ventilated BIPV facade, as described in [55]. This explains why the Ross' correlation can be a good approximation for the BIPV-CW in this work. Moreover, Figure 20a also shows that not considering temperature effects leads to overestimations in daily energy yield compared to all ventilated cases. This means that power losses related to temperature should be considered even for well-ventilated BIPV modules.

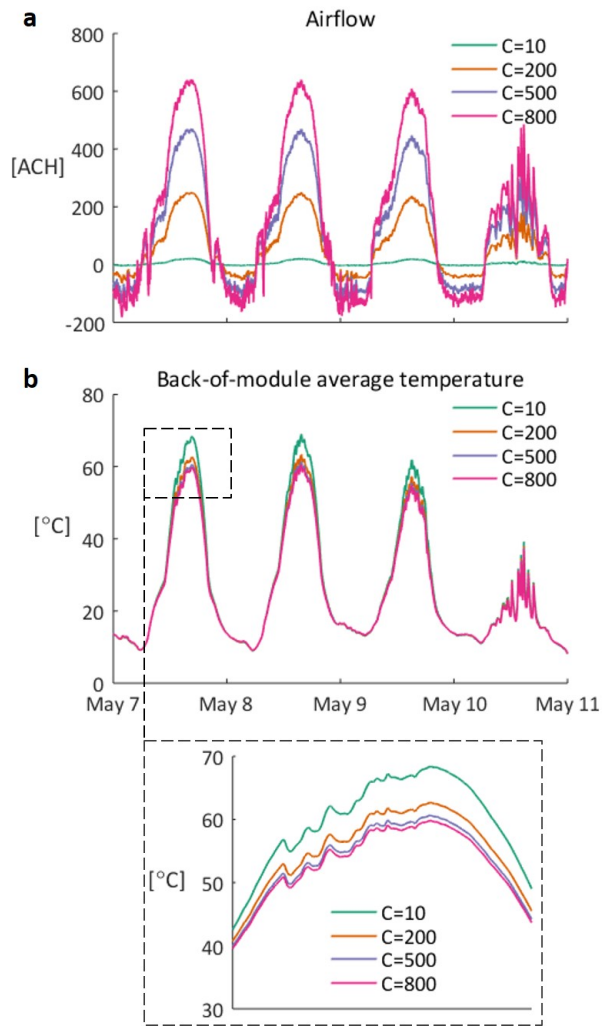


Figure 19: Impact of increasing C value on the (a) airflow rate, (b) back-of-module average temperature with zoom in mid-afternoon May 7.

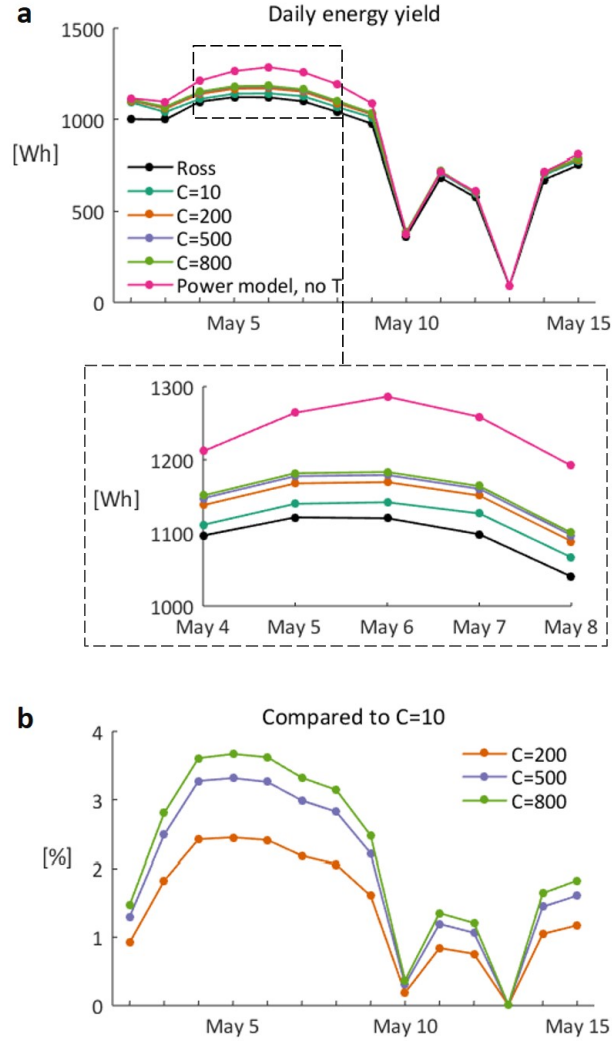


Figure 20: Impact of increasing C value: (a) daily energy yield, and (b) difference in daily energy yield compared to $C = 10$ (only ventilated cases).

4.3. Summary and recommendations

A detailed modelling of electrical, thermal and airflow aspects as employed in the multi-physics BIPV model has two implications. First, the

high-resolution electrical model employed for the simulation of intra-module shading effects demands significant computational resources. Second, the physics-based thermal and airflow models require information about the BIPV geometry, dimension, bill of materials, cavity losses, wind flow, etc. These requirements may not correspond to the needs of certain BIPV stakeholders that may benefit from a faster simulation environment, even if it means a compromise in terms of accuracy and/or flexibility. These requirements may also depend on the building design stage.

A key aspect for successful BIPV projects is to consider BIPV at the early stage in the building design [27]. At these initial stages, BIPV models should provide a fast estimate with a limited amount of data (e.g. area and efficiency). In this case, a power model combined with an empirical temperature correlation such as the ones by Ross and Skoplaki et al. are an option. Not including temperature effects is not recommended, as it results in overestimation of the BIPV output. For the particular BIPV-CW investigated in this paper, this can result in daily energy yield overestimations up to 20 % in clear sky days. Furthermore, a conservative approach could be used to consider shading losses (as presented in Section 4.1.1). A shading loss analysis using a simplified method such as proposed in [61] is also an option. The use of simplified models enables the simulation of different scenarios, without requiring a high level of detail or expertise, in terms of data or shading calculation, which could frustrate the interest in BIPV.

At the final stages of the building design, a more detailed description of the building and the BIPV system is already available. Here, the suggestion is a two-step approach. The first step is the evaluation of the BIPV thermal per-

formance within a building simulation framework. The recommended combination is the coupling between a power model and physics-based thermal and airflow models, with a conservative approach for the shading events. This reduces the total simulation time, since a high-resolution electrical model is not needed. The second step is the detailed assessment and optimisation of the electrical architecture of the whole system, including strings configuration, batteries, converters, etc. For this analysis, a high-resolution circuit-based approach and a detailed shading analysis are recommended, e.g. [22, 46]. To reduce computation time, the BIPV temperature calculated in the first step could be used as boundary condition for the temperature-dependent one-diode model. An empirical temperature correlation is also an option if the BIPV module is similar to the BIPV-CW in this work.

5. Discussion

Limitations of this work and suggestions for future work are discussed, concerning:

(1) **BIPV setup and dataset used for validation:** The results and recommendations presented in this paper concern the particular BIPV-CW element and experimental dataset described in this paper. Performing similar comparative analyses for different BIPV modules operating under different climatic conditions is essential to further verify these recommendations. Nevertheless, it must be noted that physics-based models are less dependent on the amount of data used for experimental validation (compared to data-driven and empirical correlation approaches);

(2) **Input data uncertainty:** Although this paper focuses on exper-

imental validation and comparison of different models, the uncertainty in the input data is also a concern. In a previous work by the authors [62], a probabilistic framework was developed to investigate the sensibility of the multi-physics BIPV model to variations in its inputs. The main findings indicate that exterior heat transfer and cavity ventilation are important aspects to consider in BIPV models;

(3) **Electrical modelling:** Despite the good agreement with experimental data, the electrical model could still be improved. For example, more advanced methods can be used to describe the one-diode parameters as a function of the PV operating conditions, as discussed in e.g. [41, 42, 63–65]. The use of a two-diode model is also often proposed as an improvement over the one-diode approach (e.g. [41, 42, 63–65]). More recently, data-driven approaches have also gained attention (e.g. [66–69]). However, an issue commonly raised concerning more complex numerical techniques is the risk of non-convergence in case of inappropriate initial values [41, 42]. Similarly, data-driven approaches require availability of data beforehand;

(4) **Shading effects:** A limitation of this study is that the impact of shading events could not be assessed using the experimental data obtained. However, this kind of comparison using experimental data has been carried out before in the literature (e.g. [22, 47]). These studies show that high-resolution one-diode approaches such as the one employed in this work are capable to provide accurate power predictions for PV modules under shading events. Nevertheless, future work could focus on extending the validation dataset to include shading events. For example, the shading cases proposed in Section 4.1.1 could be emulated in the BIPV-CW setup;

(5) **Thermal modelling:** Despite the relatively good agreement between results obtained using empirical temperature correlations and experimental data for the poorly-ventilated BIPV-CW, empirical correlations are only suitable to simulate BIPV configurations similar to the ones they have been derived from. In fact, an earlier work by the authors demonstrates that the empirical temperature correlations by Ross and Skoplaki et al. fail to predict the temperature of a well-ventilated BIPV module [21]. However, so far, only a few studies have provided empirical temperature correlations for facade BIPV applications (e.g. [55, 70]). If empirical temperature correlations are to be used, data from different types of BIPV modules operating under different conditions need to be collected. Ongoing work by the authors aims to provide empirical coefficients (k in Eq. 8) for the Ross model for a range of BIPV modules;

(6) **Cavity ventilation:** The results in this paper indicate that an increase in daily energy yield up to 3.6 % can be achieved. This improvement might seem minor, but the associated decrease in back-of-module temperature of about 10 °C helps to mitigate degradation effects, improving the module's lifetime. Moreover, these results are only an indication of the potential energy gain associated with enhanced ventilation. Detailed thermal and flow analysis are needed to better understand the impact of ventilation on the temperature of BIPV modules. These detailed analyses can help to identify hot spots and suitable cooling techniques, such as fins or staggering configurations. Ongoing work by the authors combines computational fluid dynamics with experimental data for this purpose.

(7) **Building performance simulations:** It is important to highlight

that the multi-physics BIPV model presented in this paper is part of a comprehensive simulation framework for the performance assessment of buildings. Different analysis can be performed using this integrated simulation environment. For example, the model has been used in previous publications by the authors to evaluate different electrical architectures for the building grid, including different levels of battery penetration [71] and to investigate the performance of BIPV facades under different climates [72].

6. Conclusion

This paper investigates how the complexity of a building integrated photovoltaic (BIPV) model affects its predictions in terms of energy yield and (back-of-module) temperature. Experimental data from a real-size c-Si BIPV curtain wall element are used to evaluate the models. The relevance of this analysis lies in the need for sound recommendations for BIPV modelling, taking into account the diversity of BIPV stakeholders with their specific needs in terms of simulation time and data availability.

Starting from a detailed multi-physics BIPV model that combines a high-resolution one-diode model with physics-based thermal and airflow models, the main findings in this paper suggest that it is possible to reduce the complexity of a BIPV model, as follows:

(1) a linear power model may be an option to replace the one-diode model for unshaded c-Si BIPV modules, such as the BIPV curtain wall treated here. For clear sky days, the linear power model provides daily energy yield estimations with an average error of 4.5 % (compared to 2 % for the detailed multi-physics BIPV model);

(2) empirical temperature correlations can be a good approximation to estimate the BIPV daily energy yield, replacing the physics-based approach, provided that the BIPV configuration is similar to the experimental data used to derive the correlation. For clear sky days, the two empirical temperature correlations used in this work provide daily energy yield estimations with an average error of 5.9 and 5.5 % (compared to 2 % for the detailed multi-physics BIPV model);

(3) a physics-based thermal-airflow model combined with either a one-diode model or a linear power model is able to predict both the BIPV daily energy yield and temperature with relatively good accuracy. A physics-based approach is particularly suitable for parametric analysis (such as varying ventilation conditions or the size of the BIPV module);

(4) not considering power losses caused by variations in cell temperature can lead to significant overestimation of the BIPV energy potential, up to about 20 % on clear sky days.

Acknowledgments

This work has been conducted within the EFRO SALK project, supported by the EU, ERDF, Flanders Innovation & Entrepreneurship and the Province of Limburg. The authors acknowledge the important collaboration with the Department of Electrical Engineering (ESAT) from KU Leuven as well as with the PV research group from imec. The authors also recognise the important role of our technicians Wim Bertels, Patricia Elsen, and Jimmy Van Criekingen, regarding the experimental work. Twan van Hooff is currently a postdoctoral fellow of the Research Foundation – Flanders (FWO)

and acknowledges its financial support (project FWO 12R9718N).

References

- [1] S. Yu, Q. Tan, M. Evans, P. Kyle, L. Vu, P. L. Patel, Improving building energy efficiency in india: State-level analysis of building energy efficiency policies, *Energy Policy* 110 (2017) 331–341.
- [2] W. Pan, M. Pan, Opportunities and risks of implementing zero-carbon building policy for cities: Hong kong case, *Applied Energy* 256 (2019) 113835.
- [3] F. Silvero, F. Rodrigues, S. Montelpare, E. Spacone, H. Varum, The path towards buildings energy efficiency in south american countries, *Sustainable Cities and Society* 44 (2019) 646–665.
- [4] EPBD, Directive 2010/31/EU of the European Parliament and of the Council of 19 May 2010 on the energy performance of buildings (recast), *Official Journal of the European Union* 18 (06) (2010) 2010.
- [5] European Commission. Clean energy for all Europeans (2019).
- [6] B. D. Leibowicz, C. M. Lanham, M. T. Brozynski, J. R. Vázquez-Canteli, N. C. Castejón, Z. Nagy, Optimal decarbonization pathways for urban residential building energy services, *Applied Energy* 230 (2018) 1311–1325.
- [7] Solar Power Europe, Solar Skins: An opportunity for greener cities, Report (2019).

- [8] N. Sánchez-Pantoja, R. Vidal, M. C. Pastor, Aesthetic perception of photovoltaic integration within new proposals for ecological architecture, *Sustainable cities and society* 39 (2018) 203–214.
- [9] C. D. Zomer, M. R. Costa, A. Nobre, R. Rüter, Performance compromises of building-integrated and building-applied photovoltaics (BIPV and bapv) in brazilian airports, *Energy and buildings* 66 (2013) 607–615.
- [10] S. Aguacil, S. Lufkin, E. Rey, Active surfaces selection method for building-integrated photovoltaics (bipv) in renovation projects based on self-consumption and self-sufficiency, *Energy and Buildings* 193 (2019) 15–28.
- [11] F. J. Osseweijer, L. B. Van Den Hurk, E. J. Teunissen, W. G. van Sark, A comparative review of building integrated photovoltaics ecosystems in selected European countries, *Renewable and Sustainable Energy Reviews* 90 (2018) 1027–1040.
- [12] E. Saretta, P. Caputo, F. Frontini, A review study about energy renovation of building facades with BIPV in urban environment, *Sustainable Cities and Society* 44 (2018) 343–355.
- [13] G. Evola, G. Margani, Renovation of apartment blocks with bipv: Energy and economic evaluation in temperate climate, *Energy and Buildings* 130 (2016) 794–810.
- [14] R. A. Agathokleous, S. A. Kalogirou, Double skin facades (DSF) and building integrated photovoltaics (BIPV): A review of configurations and heat transfer characteristics, *Renewable Energy* 89 (2016) 743–756.

- [15] T. Yang, A. K. Athienitis, A review of research and developments of building-integrated photovoltaic/thermal (BIPV/T) systems, *Renewable and Sustainable Energy Reviews* 66 (2016) 886–912.
- [16] B. Norton, P. C. Eames, T. K. Mallick, M. J. Huang, S. J. McCormack, J. D. Mondol, Y. G. Yohanis, Enhancing the performance of building integrated photovoltaics, *Solar Energy* 85 (8) (2011) 1629–1664.
- [17] E. Biyik, M. Araz, A. Hepbasli, M. Shahrestani, R. Yao, L. Shao, E. Es-sah, A. C. Oliveira, T. del Caño, E. Rico, et al., A key review of building integrated photovoltaic (BIPV) systems, *Engineering Science and Technology, an International Journal* 20 (3) (2017) 833–858.
- [18] Y. B. Assoa, F. Sauzedde, B. Boillot, Numerical parametric study of the thermal and electrical performance of a BIPV/T hybrid collector for drying applications, *Renewable energy* 129 (2018) 121–131.
- [19] D. Thevenard, Review and recommendations for improving the modelling of building integrated photovoltaic systems, in: *Proceedings of the 9th International IBPSA Conference, Montreal, Canada, Citeseer, 2005*.
- [20] N. Pajkic, M. Kragh, J. Yang, P. Wijeratne Mudiyansele, P. Wijeratne Mudiyansele, E. Too, R. Wakefield, et al., *BIPV design and performance modelling: Tools and methods* (2019).
- [21] J. E. Goncalves, T. van Hooff, D. Saelens, A physics-based high-resolution BIPV model for building performance simulations, *Solar Energy* 204 (2020) 585–599.

- [22] L. Walker, J. Hofer, A. Schlueter, High-resolution, parametric BIPV and electrical systems modeling and design, *Applied Energy* 238 (2019) 164–179.
- [23] H. Alrashidi, A. Ghosh, W. Issa, N. Sellami, T. K. Mallick, S. Sundaram, Thermal performance of semitransparent cdte BIPV window at temperate climate, *Solar Energy* 195 (2020) 536–543.
- [24] H. M. Lee, J. H. Yoon, Power performance analysis of a transparent dssc BIPV window based on 2 year measurement data in a full-scale mock-up, *Applied Energy* 225 (2018) 1013–1021.
- [25] Y.-B. Assoa, C. Ménézo, Dynamic study of a new concept of photovoltaic–thermal hybrid collector, *Solar energy* 107 (2014) 637–652.
- [26] R. A. Agathokleous, S. A. Kalogirou, Part i: Thermal analysis of naturally ventilated BIPV system: Experimental investigation and convective heat transfer coefficients estimation, *Solar Energy* 169 (2018) 673–681.
- [27] P. Macé, L. David, J. Benson, Transition towards Sound BIPV Business Models (2018).
- [28] M. Brito, S. Freitas, S. Guimarães, C. Catita, P. Redweik, The importance of facades for the solar PV potential of a Mediterranean city using LiDAR data, *Renewable Energy* 111 (2017) 85–94.
- [29] S. Freitas, M. Brito, Non-cumulative only solar photovoltaics for electricity load-matching, *Renewable and Sustainable Energy Reviews* 109 (2019) 271–283.

- [30] J. P. Bentley, Principles of measurement systems, Harlow: Addison Wesley Longman Ltd., 1995.
- [31] D. Saelens, Energy performance assessment of single storey multiple-skin facades, Ph.D. thesis, KU Leuven (2002).
- [32] A. A. AlWaaly, M. C. Paul, P. S. Dobson, Effects of thermocouple electrical insulation on the measurement of surface temperature, Applied Thermal Engineering 89 (2015) 421–431.
- [33] B. Herteleer, Outdoor thermal and electrical characterisation of photovoltaic modules and systems, Ph.D. thesis, KU Leuven (2016).
- [34] R. Baetens, R. De Coninck, F. Jorissen, D. Picard, L. Helsen, D. Saelens, OpenIDEAS - an open framework for integrated district energy simulations, in: Building simulation, 2015.
- [35] F. Jorissen, G. Reynders, R. Baetens, D. Picard, D. Saelens, L. Helsen, Implementation and verification of the IDEAS building energy simulation library, Journal of Building Performance Simulation (2018) 1–20.
- [36] J. Falk, K. Sandin, Ventilated rainscreen cladding: Measurements of cavity air velocities, estimation of air change rates and evaluation of driving forces, Building and Environment 59 (2013) 164–176.
- [37] J. Langmans, S. Roels, Experimental analysis of cavity ventilation behind rainscreen cladding systems: A comparison of four measuring techniques, Building and Environment 87 (2015) 177–192.
- [38] V. L. Streeter, E. B. Wylie, Fluid Mechanics, McGraw-Hill, 1983.

- [39] J. Straube, E. Burnett, Vents, ventilation, and pressure moderation, University of Waterloo Building Engineering Group Report for Canada Mortgage and Housing Corporation, Ottawa, Ontario (1995).
- [40] J. J. Roberts, A. A. M. Zevallos, A. M. Cassula, Assessment of photovoltaic performance models for system simulation, *Renewable and Sustainable Energy Reviews* 72 (2017) 1104–1123.
- [41] V. J. Chin, Z. Salam, K. Ishaque, Cell modelling and model parameters estimation techniques for photovoltaic simulator application: A review, *Applied Energy* 154 (2015) 500–519.
- [42] G. Ciulla, V. L. Brano, V. Di Dio, G. Cipriani, A comparison of different one-diode models for the representation of i–v characteristic of a pv cell, *Renewable and Sustainable Energy Reviews* 32 (2014) 684–696.
- [43] H.-L. Tsai, Insolation-oriented model of photovoltaic module using matlab/simulink, *Solar energy* 84 (7) (2010) 1318–1326.
- [44] V. d’Alessandro, F. Di Napoli, P. Guerriero, S. Daliento, An automated high-granularity tool for a fast evaluation of the yield of pv plants accounting for shading effects, *Renewable Energy* 83 (2015) 294–304.
- [45] J. Hofer, A. Groenewolt, P. Jayathissa, Z. Nagy, A. Schlueter, Parametric analysis and systems design of dynamic photovoltaic shading modules, *Energy Science & Engineering* 4 (2) (2016) 134–152.
- [46] W. Sprenger, H. R. Wilson, T. E. Kuhn, Electricity yield simulation for the building-integrated photovoltaic system installed in the main

- building roof of the fraunhofer institute for Solar Energy systems ise, *Solar Energy* 135 (2016) 633–643.
- [47] S. Gallardo-Saavedra, B. Karlsson, Simulation, validation and analysis of shading effects on a pv system, *Solar Energy* 170 (2018) 828–839.
- [48] H. Goverde, D. Goossens, J. Govaerts, F. Catthoor, K. Baert, J. Poortmans, J. Driesen, Spatial and temporal analysis of wind effects on PV modules: Consequences for electrical power evaluation, *Solar Energy* 147 (2017) 292–299.
- [49] I. T. Horváth, H. Goverde, P. Manganiello, J. Govaerts, L. Tous, B. Aldalali, E. Vörösházi, J. Szlufcik, F. Catthoor, J. Poortmans, Photovoltaic energy yield modelling under desert and moderate climates: What-if exploration of different cell technologies, *Solar Energy* 173 (2018) 728–739.
- [50] J. Brkic, M. Ceran, M. Elmoghazy, R. Kavlak, A. Haumer, C. Kral, Open source photovoltaics library for systemic investigations, in: Proceedings of the 13th International Modelica Conference, Regensburg, Germany, March 4–6, 2019, no. 157, Linköping University Electronic Press, 2019.
- [51] D. Anagnostos, H. Goverde, F. Catthoor, D. Soudris, J. Poortmans, Systematic cross-validation of photovoltaic energy yield models for dynamic environmental conditions, *Solar Energy* 155 (2017) 698–705.
- [52] E. Piccoli, A. Dama, A. Dolara, S. Leva, Experimental validation of

- a model for pv systems under partial shading for building integrated applications, *Solar Energy* 183 (2019) 356–370.
- [53] R. Ross Jr, Interface design considerations for terrestrial solar cell modules, in: *12th Photovoltaic Specialists Conference*, 1976, pp. 801–806.
- [54] E. Skoplaki, J. A. Palyvos, Operating temperature of photovoltaic modules: A survey of pertinent correlations, *Renewable energy* 34 (1) (2009) 23–29.
- [55] T. Nordmann, L. Clavadetscher, Understanding temperature effects on PV system performance, in: *3rd World Conference on Photovoltaic Energy Conversion*, 2003. *Proceedings of*, Vol. 3, IEEE, 2003, pp. 2243–2246.
- [56] E. Skoplaki, A. Boudouvis, J. Palyvos, A simple correlation for the operating temperature of photovoltaic modules of arbitrary mounting, *Solar Energy Materials and Solar Cells* 92 (11) (2008) 1393–1402.
- [57] D. Saelens, H. Hens, Experimental evaluation of airflow in naturally ventilated active envelopes, *Journal of Thermal Envelope and Building Science* 25 (2) (2001) 101–127.
- [58] L. E. Nevander, B. Elmarsson, *Fukthandbok: praktik och teori*, Svensk byggtjänst, 1994.
- [59] C. Gudum, C. Rode, Moisture transport and convection in building envelopes, Ph.D. thesis, Technical University of Denmark, Denmark (2003).

- [60] O. Dupré, R. Vaillon, M. A. Green, Thermal behavior of photovoltaic devices, *Physics and Engineering* 10 (2017) 978–3.
- [61] C. Zomer, R. Rüther, Simplified method for shading-loss analysis in BIPV systems—part 1: Theoretical study, *Energy and Buildings* 141 (2017) 69–82.
- [62] J. E. Gonçalves, T. van Hooff, D. Saelens, Understanding the behaviour of naturally-ventilated BIPV modules: A sensitivity analysis, *Renewable Energy* 161 (2020) 133–148. doi:<https://doi.org/10.1016/j.renene.2020.06.086>.
- [63] M. A. Hasan, S. K. Parida, An overview of solar photovoltaic panel modeling based on analytical and experimental viewpoint, *Renewable and Sustainable Energy Reviews* 60 (2016) 75–83.
- [64] A. M. Humada, M. Hojabri, S. Mekhilef, H. M. Hamada, Solar cell parameters extraction based on single and double-diode models: A review, *Renewable and Sustainable Energy Reviews* 56 (2016) 494–509.
- [65] A. R. Jordehi, Parameter estimation of solar photovoltaic (pv) cells: A review, *Renewable and Sustainable Energy Reviews* 61 (2016) 354–371.
- [66] J. Antonanzas, N. Osorio, R. Escobar, R. Urraca, F. J. Martinez-de Pison, F. Antonanzas-Torres, Review of photovoltaic power forecasting, *Solar Energy* 136 (2016) 78–111.
- [67] G. Graditi, S. Ferlito, G. Adinolfi, G. M. Tina, C. Ventura, Energy yield estimation of thin-film photovoltaic plants by using physical approach and artificial neural networks, *Solar Energy* 130 (2016) 232–243.

- [68] S. Ferlito, G. Adinolfi, G. Graditi, Comparative analysis of data-driven methods online and offline trained to the forecasting of grid-connected photovoltaic plant production, *Applied Energy* 205 (2017) 116–129.
- [69] R. Castro, Data-driven pv modules modelling: Comparison between equivalent electric circuit and artificial intelligence based models, *Sustainable Energy Technologies and Assessments* 30 (2018) 230–238.
- [70] C. Toledo, R. López-Vicente, J. Abad, A. Urbina, Thermal performance of pv modules as building elements: analysis under real operating conditions of different technologies., *Energy and Buildings* (2020) 110087.
- [71] K. Spiliotis, J. E. Gonçalves, D. Saelens, K. Baert, J. Driesen, Electrical system architectures for building-integrated photovoltaics: A comparative analysis using a modelling framework in modelica, *Applied Energy* 261 (2020) 114–247. doi:10.1016/j.apenergy.2019.114247.
- [72] J. E. Gonçalves, T. van Hooff, D. Saelens, Performance of BIPV modules under different climatic conditions, *Journal WEENTECH Proceedings in Energy* (2019) 107–115.